A W Boson Mass Measurement Using the Ratio of Transverse Masses of the W and Z Bosons in $p\bar{p}$ Collisions at $\sqrt{s}$ =1.8 TeV with the DØ Detector

A Dissertation Presented
by

Dennis Leonidovich Shpakov

to
The Graduate School

in Partial Fulfillment of the
Requirements
for the Degree of
Doctor of Philosophy
in
Physics

State University of New York
at
Stony Brook

August 2000

Abstract of the Dissertation

A W Boson Mass Measurement Using the Ratio of Transverse Masses of the W and Z Bosons in $p\bar{p}$ Collisions at $\sqrt{s}$ =1.8 TeV with the DØ Detector

by
Dennis Leonidovich Shpakov

Doctor of Philosophy
in
Physics

State University of New York
at Stony Brook

2000

This dissertation reports on the measurement of the W boson mass from a direct determination of the ratio of the transverse masses of W and Z bosons using the DØ detector at the Tevatron collider at Fermilab. The analysis is based on the $W \to e\nu$ and $Z \to e^+e^-$ decay modes.

In the standard DØ W boson mass measurement method the transverse mass

distribution of the $W \to e\nu$ decay products is compared to Monte Carlo templates for a set of input W mass values, and a sample of Z events is used for the calibration of electron and hadronic energy. The ratio method compares the transverse mass of the W sample directly to the scaled transverse mass of the Z sample. The comparison is based on the assumption that the transverse mass of the two decay products is insensitive to the production and decay mechanism of the two bosons but depends on the mass of the parent boson. If the $M_{\mathrm{T}}(Z)$ distribution is scaled down by a factor of $M(W)/M(Z)$, the new distribution would be identical to that of $M_{\mathrm{T}}(W)$ for ideally measured transverse momenta of the decay products. The W mass is given by the product of the Z mass measured precisely at the LEP collider at CERN and the scale factor that optimizes the Kolmogorov–Smirnov probability for the two transverse mass distributions corrected for the detector acceptance and energy resolution.

As compared to the standard DØ W mass analysis, the ratio method is less sensitive to uncertainties in the W and Z production model but has a larger statistical error due to a limited sample of Z events. The overall performance of the ratio method is expected to be competitive with the that of the conventional method in Run II of the Tevatron collider.

This study corresponds to an integrated luminosity of $82\,\mathrm{pb}^{-1}$ acquired by the DØ detector during the Tevatron collider Run Ib (1994–1995). The data samples have been collected in both central and forward region of the detector. The W boson mass

is found to be:

$$m_W = 80.115 \pm 0.211(\text{stat.}) \pm 0.050(\text{syst.})\,\text{GeV}.$$

To my parents

Contents

Abstract **iii**

Acknowledgements **xxi**

1 Introduction **1**

1.1 Fundamental Particles in the Standard Model 1

1.2 Motivation for Precision Measurement of the W Boson Mass 2

1.3 W Boson Production in $p\bar{p}$ Collisions 5

1.4 W Boson Decay 7

2 Experimental Apparatus **11**

2.1 Fermilab Accelerator Complex 11

2.2 Overview of the DØ Detector. DØ Coordinate System 15

2.2.1 General Design and Purpose 15

2.2.2 DØ Coordinate System 16

2.3 Central Detector 18

2.3.1 Drift Chamber Operation Principle 19

2.3.2 Vertex Chamber (VTX) 20

2.3.3 Transition Radiation Detector (TRD) 21

2.3.4 Central Drift Chamber (CDC) 22

2.3.5 Forward Drift Chambers (FDC) 23

2.4 Calorimeters 24

2.4.1 General Design and Operation Principle 24

2.4.2 Central Calorimeter 28

2.4.3 End Calorimeters 29

2.4.4 Inter-cryostat Detectors and Massless Gaps 29

2.4.5 Calorimeter Energy and Position Resolution 30

2.5 Muon System 31

2.5.1 General Design 31

2.5.2 Wide Angle Muon Spectrometers (WAMUS) 31

2.5.3 Small Angle Muon Spectrometers (SAMUS) 32

2.6 Trigger and Data Acquisition 33

2.6.1 Trigger and Data Acquisition System Overview 33

2.6.2 Level 0 (L0) Trigger 33

2.6.3 Level 1 (L1) and Level 1.5 (L1.5) Trigger 34

2.6.4 Level 2 (L2) Trigger 35

2.6.5 Main Ring Veto Triggers 35

3 Event Reconstruction and Particle Identification 39

3.1 DØRECO Program 39

3.2 Track Reconstruction and Vertex Finding 40

3.3 Energy Measurement in the Calorimeter 42

3.4 Electron and Photon Reconstruction 43

3.4.1 Clustering Algorithm 43

3.4.2 Electromagnetic Energy Fraction and Isolation Fraction 45

3.4.3 Shower Shape — The Covariance Matrix 46

3.4.4 Ionization Energy Loss 47

3.4.5 Track Match Significance 47

3.4.6 TRD Efficiency 48

3.5 Missing Energy 49

3.6 Jet Reconstruction 50

4 Analysis Procedure 53

4.1 A Fast W and Z Monte Carlo Generator 53

4.1.1 Vector Boson Production Model 54

4.1.2 Boson Decay 57

4.1.3 Parameterized Detector Model 57

4.2 Overview of the Ratio Method 58

4.2.1 Kinematic Observables Used in the W Boson Mass Analysis . 58

4.2.2 Ratio of Transverse Masses of the W and Z Bosons 59

4.2.3 Kolmogorov–Smirnov Test 62

5 Understanding Detector Response 65

5.1 Energy Scale and Resolution 65

5.1.1 Electron Energy Scale 65

5.1.2 Electron Resolution 68

5.1.3 Hadronic Energy Scale and Neutrino Energy 69

5.1.4 Hadronic Energy Resolution 72

5.1.5 Procedure for Applying Energy Response and Resolution Corrections 73

5.2 Event Selection Efficiency 74

5.3 Detector Acceptance Effects on the Mass Ratio 75

5.3.1 η Dependent Weight 76

5.3.2 φ Dependent Weight 80

5.4 Monte Carlo Tests 80

6 Data Analysis and Study of Systematics 85

6.1 Data Selection 85

6.1.1 Online Event Selection 86

6.1.2 Kinematic Cuts on Electron Candidates 86

6.1.3 Fiducial Cuts 86

6.1.4 Event Selection Criteria 87

6.2 Kolmogorov–Smirnov Fit for the Data 89

6.3 Systematic Uncertainties 93

6.3.1 W and Z Production and Decay 93

6.3.2 Detector Response Parameters 96

6.3.3 Backgrounds 101

6.3.4 Summary of the Systematics 101

7 Summary of Results and Conclusion 103

7.1 W Mass from the Ratio Fit and from the Standard DØ Method . . . 103

7.2 The Future 104

A Event Reconstruction Algorithms for the Forward Preshower Detector 107

A.1 General Design of the Forward Preshower Detector 107

A.2 FPS Event Reconstruction Process 109

A.3 Software Implementation 112

A.3.1 Hierarchy of FPS Offline Packages 112

A.3.2 FPS Geometry Description 113

A.4 Algorithm Performance 115

A.5 Conclusion 118

List of Figures

1.1 Loop diagrams contributing to radiative corrections Δr: left — top quark diagram, right — Higgs boson diagram 4

1.2 The Higgs boson mass *vs.* the mass of the top quark and W boson . . 5

1.3 W boson production at the lowest order 6

1.4 W boson production at the first order in α_s 6

1.5 Lowest order diagram of the $W \to e\nu$ decay 9

2.1 Fermilab accelerator complex 12

2.2 3–D view of the DØ detector 16

2.3 Side view of the DØ detector 17

2.4 DØ coordinate system 18

2.5 DØ central detector 20

2.6 (r, φ) view of the vertex chamber 21

2.7 Transition radiation detector 22

2.8 End view of the central drift chamber 23

2.9 Forward drift chamber 24

2.10 Cut-away view of the DØ calorimeter 26

2.11 One quadrant of the calorimeter showing the arrangement of cells and towers 27

2.12 Calorimeter cell 28

2.13 Muon system 32

2.14 DØ trigger system 37

4.1 Mass distribution from `HERWIG` using the MRSA pdf showing the parton luminosity effect (plot from I. Adam [34]) 56

4.2 Distributions of the transverse mass of the W boson (left) and transverse momentum of the electron: solid histograms — $p_{\mathrm{T}}^{\mathrm{boson}} = 0$, dots — with correct $p_{\mathrm{T}}^{\mathrm{boson}}$ distribution, shaded area — with detector effects. 59

4.3 Transverse mass of the W boson (solid histogram) and scaled transverse mass of the Z boson (dots). Lower plot shows the bin-by-bin difference between the two distributions over the error with the horizontal band corresponding to the $\pm 2\sigma$ difference. This will be a standard convention further on. The disagreement between the two distributions at the peak is due to the production and decay effects. 61

4.4 W transverse mass (left), electron p_{T} (center), and neutrino p_{T} W distributions for two choices of pdfs, CTEQ2M (solid line) and MRSD$-'$ (dots). The bottom part of each plot shows the bin by bin difference between the two spectra divided by the error, and the horizontal band corresponds to ± 2 standard deviations 62

4.5 Kolmogorov–Smirnov probability as a function of the running difference between two distributions 63

4.6 Kolmogorov–Smirnov probability for $M_{\mathrm{T}}(W)$ and scaled $M_{\mathrm{T}}(Z)$ as a function of the scale factor 64

5.1 Difference between the energy measured in the calorimeter, E, and the beam momentum, p, over the beam momentum, as a function of p . . 66

5.2 Momentum vectors in the transverse plane for the W event. $U_{\|}$ is the projection of the hadronic transverse momentum U_{T} onto the transverse direction of the electron 67

5.3 U^{ue} deviation from the nominal value in the central (left) and forward calorimeter 68

5.4 Minimum bias transverse momentum distribution. Left — for the instantaneous luminosity range from 0 to $10^{30}\,\mathrm{cm}^{-2}\mathrm{s}^{-1}$, right — from $1.6 \cdot 10^{31}\,\mathrm{cm}^{-2}\mathrm{s}^{-1}$ to $2.5 \cdot 10^{31}\,\mathrm{cm}^{-2}\mathrm{s}^{-1}$ 73

5.5 Calculation of probability for a single electron (W) event to be detected by the calorimeter. The Gaussian represents the experimental vertex distribution, the dashed lines show the projections of the CC and EC boundaries onto the z axis at angle θ of the electron. The event is detected if the vertex position is within the shaded region. 76

5.6 Event detection probability: left — as a function of the electron η for the W events, right — as a function of pseudorapidities of the two electrons for the Z events 77

5.7 Pseudorapidity distributions of the second Z electron (left plots) and Kolmogorov–Smirnov probability as a function of the W mass with and without fiducial cuts and acceptance weights 79

5.8 Transverse mass of the W boson (solid) and scaled transverse mass of the Z boson (dots). The scale factor here and on the other plots corresponds to the maximum Kolmogorov–Smirnov probability 81

5.9 p_{T} of the boson. The discrepancy between the two distributions at high p_{T} values is due to the different masses and production mechanisms of the two bosons (different parton distributions of u and v quarks). . . 81

5.10 Left — p_{T} of the electron (scaled for the Z), right — p_{T} of the W neutrino on top of the scaled p_{T} of the second Z electron. Solid line — W, points — Z 82

5.11 Pseudorapidity of the W and Z electrons 83

5.12 Kolmogorov–Smirnov probability as a function of the W mass for 100 Z extra smearing iterations 84

5.13 Mean (left) and RMS (right) values of the Kolmogorov–Smirnov probability function. The mean and r. m. s. values for the left and right plots are 80.384 ± 0.023 GeV and 0.045 ± 0.008 GeV, respectively . . . 84

6.1 W electron p_{T} and η distributions. Solid histogram — CMS Monte Carlo, points — data 88

6.2 Z electron p_{T} and η distributions. Solid histogram — CMS Monte Carlo, points — data 89

6.3 Transverse mass of the W boson (solid) and scaled transverse mass of the Z boson (dots) 90

6.4 Transverse momentum of the W and Z (scaled) bosons 90

6.5 Left — p_{T} of the electron, right — p_{T} of the W neutrino on top of p_{T} of the second Z electron. Z distributions are scaled down by the mass ratio 91

6.6 Pseudorapidity of the W and Z electrons 91

6.7 Mean (top) and RMS (bottom) values of the Kolmogorov–Smirnov probability function 92

6.8 Distribution of the output Monte Carlo W mass for 50 (W, Z) sample pairs of approximately the same sizes as data for the input mass of 80.4 GeV. 93

A.1 FPS detector quarter view in the $r - z$ plane and a close-up view of two layers of triangular scintillator strips 108

A.2 Schematic $x - y$ view of strips of one stereo layer of a FPS module. The z axis is perpendicular to the plane of the drawing and completes the right-handed system. 109

A.3 Intersection point of a u and a v cluster 111

A.4 FPS geometry tree. The two identical top level branches correspond to the north and south FPS detectors (only the north is shown). Each detector unit has four "daughter" layers, and each layer holds eight "daughter" wedges. 114

A.5 Single electron θ residuals before (left) and after the lead absorber . . 115

A.6 Single electron φ residuals before (left) and after the lead absorber. The two peaks are due to the magnetic field 116

A.7 Energy correlation between the reconstructed clusters and digitized strips 116

A.8 FPS module overlap in (x, y) plane (global DØ coordinates) 117

List of Tables

1.1 Properties of fundamental particles in the Standard Model 3

1.2 Decay modes of the W boson and their branching fractions 7

5.1 Electron energy scale parameters 66

5.2 Electron energy resolution model parameters 69

5.3 W and Z event selection efficiencies 75

6.1 W mass *vs.* Γ_W dependence. Each mass value from the right column carries a Monte Carlo statistical error of 10 MeV. This uncertainty is added in quadrature to the total systematic error. 95

6.2 W mass *vs.* dependence on the parton distribution function. Each mass value has a 10 MeV error due to Monte Carlo statistics. 95

6.3 m_W shift due to variations of the final state radiation parameters . . 96

6.4 Systematic errors on the W mass due to theoretical uncertainties . . 96

6.5 Systematic errors on the W mass due to the detector response uncertainties 100

6.6 Systematic errors on the W mass due to backgrounds 101

Acknowledgements

First, I would like to thank my advisor Michael Rijssenbeek for his support, care, guidance, and patience throughout my Stony Brook years. Fortunately for me, his wisdom and insight was not limited to physics issues but covered all sorts of my interactions with both the University and the outside world, and helped to resolve issues that sometimes came about as a result of such interactions.

My physics analysis work would hardly be possible without long hours of discussions with Ashutosh Kotwal and Srini Rajagopalan who introduced me to the details of the W mass measurement and helped a lot after that.

I moved to Fermilab at exactly the right time to have a chance to see both Run I physics and the upgrade. It was a great pleasure to work on the Forward Preshower simulations and software with Jon Kotcher, Serban Protopopescu, John Hobbs, Arnaud Lucotte, Mrinmoy Bhattacharjee and others, who helped me make an adventure as well as educational experience out of thousands of lines of C++ (and even Fortran) code.

My special thanks should go to Dean Schamberger, who is equally great at solving both hardware and software problems and enlightening the Stony Brook group at DØ on virtually everything from particle detectors to the Fermilab policy on computing.

Speaking of the Stony Brook people at DØ, I have to thank Dhiman Chakraborty for being the one who met me at DØ and showed around when I first came to Fermilab back in 1995. I should also mention that when I started to think of writing a thesis and moving on, it was Dhiman who helped me put those incoherent dreams into reality.

Slava Kulik deserves special thanks for being conveniently located next to my desk, providing links to data files and analysis code of the W mass group and for lots of useful discussions we had, including (but not limited to) those on the W mass analysis.

Finally, I would like to thank my Mom and Dad, Maksim, Nastya, Grandmas, and my friends around the world for providing the meaning of life and motivation.

Chapter 1

Introduction

1.1 Fundamental Particles in the Standard Model

Advancement of fundamental physics over the twentieth century has evolved into a beautiful theory of fundamental particles and forces called the Standard Model [1, 2, 3, 4]. The Standard Model is a quantum field theory which describes particles in terms of excited states of quantum fields. It is based on the $SU(3) \otimes SU(2) \otimes U(1)$ symmetry group, the $SU(3)$ group describing the strong color interaction, and the weak isospin and hypercharge group $SU(2) \otimes U(1)$ — the electroweak interactions.

The following three types of the fundamental particles exist in the Standard Model:

Spin 1/2 **fundamental fermions** are the building blocks of matter. They are subdivided into the quarks and leptons. Unlike the leptons, the quarks are subject

to the strong interaction, and both the quarks and leptons engage in the electroweak interaction.

Spin 1 **gauge bosons** carrying interactions between the fermions.

Spin 0 **Higgs boson** which is responsible for the spontaneous symmetry breaking and the masses of the gauge bosons and fundamental fermions in the electroweak sector of the Standard Model. The Higgs boson remains the only particle in the Standard Model yet to be observed experimentally.

Table 1.1 summarizes the fundamental particles of the Standard Model and their basic properties [4].

1.2 Motivation for Precision Measurement of the W Boson Mass

In the Standard Model the mass of the W boson is related to other electroweak parameters by the following equation [5]:

$$M_W = \sqrt{\frac{\pi\alpha(M_Z^2)}{\sqrt{2}G_{\mathrm{F}}}}\frac{1}{\sin\theta_{\mathrm{W}}\sqrt{1-\Delta r}}, \tag{1.1}$$

where θ_{W} is the weak mixing angle, M_Z is the Z boson mass which is precisely measured by the LEP collider experiments at CERN [6], G_{F} is the Fermi constant [7],

	Name	Electric charge	Mass, MeV
Leptons Spin 1/2	$\boldsymbol{e}$	-1	$0.51099907 \pm 0.00000015$
	$\boldsymbol{\mu}$	-1	105.658389 ± 0.000034
	$\boldsymbol{\tau}$	-1	$1777.05^{+0.29}_{-0.26}$
	$\boldsymbol{\nu_e}$	0	$< 1.5 \cdot 10^{-7}$
	$\boldsymbol{\nu_\mu}$	0	< 0.17
	$\boldsymbol{\nu_\tau}$	0	< 18.2
Quarks Spin 1/2	$\boldsymbol{u}$	$2/3$	$1.5 \ldots 5$
	$\boldsymbol{d}$	$-1/3$	$2 \ldots 6$
	$\boldsymbol{c}$	$2/3$	$(1.1 \ldots 1.4) \cdot 10^3$
	$\boldsymbol{s}$	$-1/3$	$60 \ldots 170$
	$\boldsymbol{t}$	$2/3$	$(174.3 \pm 5.1) \cdot 10^3$
	$\boldsymbol{b}$	$-1/3$	$4.1 \cdot 10^3 \ldots 4.4 \cdot 10^3$
Gauge bosons Spin 1	γ	0	0
	$\boldsymbol{g}$	0	0
	$\boldsymbol{W^\pm}$	± 1	$(80.41 \pm 0.10) \cdot 10^3$
	$\boldsymbol{Z}$	0	$(91.188 \pm 0.007) \cdot 10^3$
Higgs Boson Spin 0	$\boldsymbol{H^0}$	0	$> 7.75 \cdot 10^4$

Table 1.1: Properties of fundamental particles in the Standard Model

and α is the electromagnetic coupling constant. Experimental measurements of these parameters constrain radiative corrections Δr. The dominant contributions to Δr are the loop diagrams from the top quark and the Higgs boson shown in Fig. 1.1. The corrections depend on the Higgs and top masses in the following way [8, 9, 10]:

$$\Delta r \simeq \Delta\alpha + \frac{G_{\mathrm{F}}}{8\sqrt{2}\pi^2}\left[-3M_t^2 \cot^2\theta_{\mathrm{W}} + \frac{11}{3}M_W^2 \ln\frac{M_H^2}{M_W^2}\right], \tag{1.2}$$

where $\Delta\alpha \simeq 1 - \alpha/\alpha(M_Z^2) \simeq 0.06$ is a correction due to the running of the electromagnetic coupling constant.

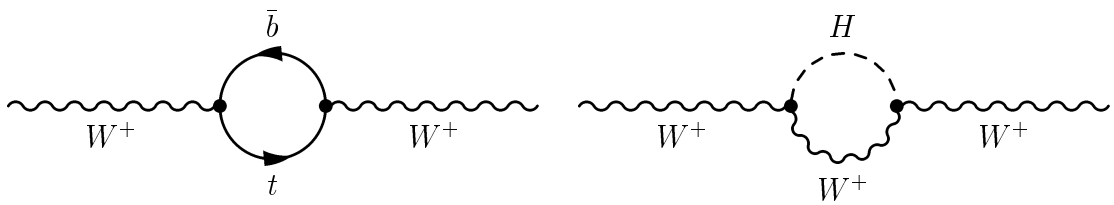

Figure 1.1: Loop diagrams contributing to radiative corrections Δr: left — top quark diagram, right — Higgs boson diagram

Fig. 1.2 shows the allowed region for the Higgs boson mass constrained by the current experimental data [11, 12]. A precision measurement of the mass of the W boson, along with the top quark mass [13], is therefore essential for future searches of the Higgs boson and tests of the Standard Model.

If the Higgs boson is discovered and its mass measured in the upgraded Tevatron or LHC experiments, comparison between the measured mass and the value calculated from the top and W mass would be an important cross-check of the Standard Model [14]. A discrepancy between the two values may indicate a presence of a new physics. Corrections to the W mass in the Minimal Supersymmetric Model — one of the popular extensions to the Standard Model — have been studied by Pierce *et al.* [15].

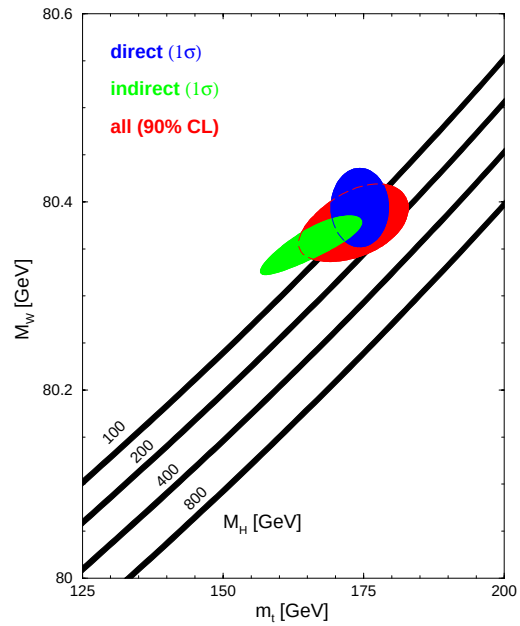

Figure 1.2: The Higgs boson mass *vs.* the mass of the top quark and W boson

1.3 W Boson Production in $p\bar{p}$ Collisions

The dominant production mechanism for the W bosons at the Tevatron collider is the Drell–Yan process of annihilation of a quark and an antiquark [16]. Fig. 1.3 shows the lowest order W production diagram, and Fig. 1.4 — processes including the first order corrections in the strong coupling constant α_s where the W production is accompanied by a gluon or a quark jet.

For a specific initial state of the Drell–Yan process, the W^+ production cross section is [17]

$$\hat{\sigma}(q\bar{q}' \to W^+) = 2\pi |V_{q\bar{q}'}|^2 \frac{G_{\mathrm{F}}}{\sqrt{2}} M_W^2 \delta(\hat{s} - M_W^2), \tag{1.3}$$

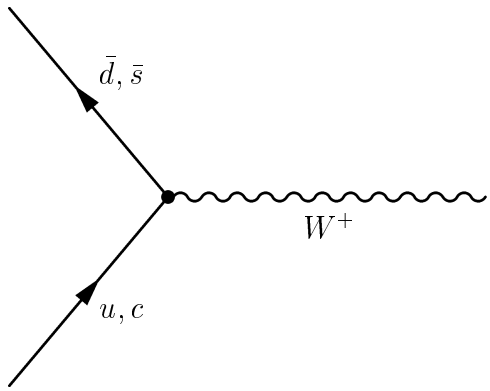

Figure 1.3: W boson production at the lowest order

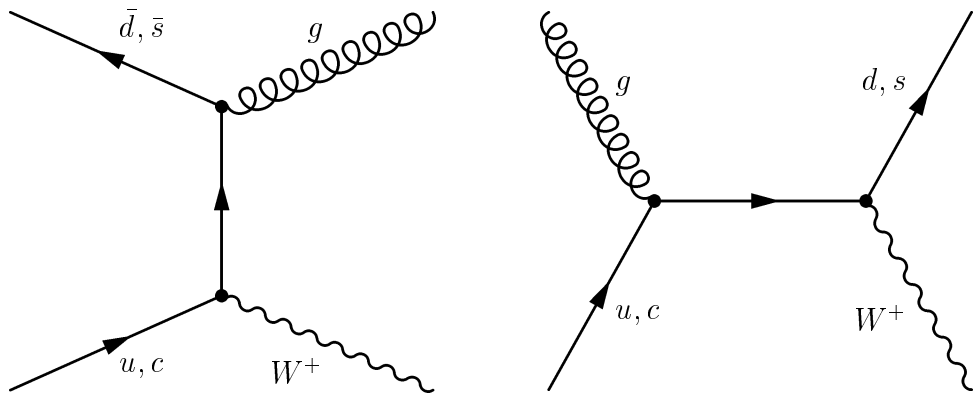

Figure 1.4: W boson production at the first order in α_s

where $\hat{s}$ is the square of the center of mass energy of the quark–antiquark system, and $|V_{q\bar{q}'}|$ is the Cabibbo–Kobayashi–Maskawa matrix element. The inclusive W production cross section is given by

$$\sigma(p\bar{p} \to W + X) = \frac{2K}{3} \int_0^1 dx_a \int_0^1 dx_b \sum_{q,\bar{q}'} q(x_a, M_W^2)\bar{q}'(x_b, M_W^2)\hat{\sigma}_{q\bar{q}'}, \tag{1.4}$$

where $\hat{\sigma}_{q\bar{q}'}$ is the cross section of the $q\bar{q}' \to W^+$ process defined by Equation 1.3,

x_a and x_b are the momentum fractions of quark q in the proton and antiquark $\bar{q}'$ in the antiproton, $q(x_a, M_W^2)$ and $\bar{q}'(x_b, M_W^2)$ are the structure functions describing the probability to find the quark in the state with momentum fraction x_a and the antiquark in the state with momentum fraction x_b, respectively. The factor of 2 is due to the sum over the two possible charges of the final state, and 1/3 is the color factor. Factor $K \simeq 1$ is a weak function of energy absorbing the QCD corrections [18].

Discussion of the production model of the W and Z bosons will continue in Section 4.1.1.

1.4 W Boson Decay

A W boson decays within $\sim 10^{-25}$ seconds width into a quark-antiquark or a lepton-neutrino pair. Table 1.2 shows the possible decay modes of the W boson with the corresponding branching fractions [4]. The hadronic decay channel is difficult to pursue experimentally because of the large background from directly produced dijets. The τ mostly decays hadronically, so this channel is also contaminated with back-

W^+ Decay Mode	Branching Fraction
$e^+\nu_e$	10.9±0.4%
$\mu^+\nu_\mu$	10.2±0.5%
$\tau^+\nu_\tau$	11.3±0.8%
$q\bar{q}'$	67.8±1.0%

Table 1.2: Decay modes of the W boson and their branching fractions

ground, and the uncertainty in the jet energy scale does not allow to make a precise mass measurement. Since the DØ detector does not have a good momentum resolution for high p_{T} muons, the muon mode does not make a precise mass measurement possible either. Therefore, only the electron channel can be used to measure the W boson mass in DØ[1].

The leading order diagram for the $W \to e\nu$ process is shown in Fig. 1.4. The angular distribution of the decay products in the W rest frame is given by

$$\mathcal{P}(\theta) \propto (1 - \lambda Q \cos\theta)^2, \tag{1.5}$$

where $\lambda = \pm 1$ is the boson helicity assumed to be aligned along the $p\bar{p}$ axis, Q is the boson charge, and θ is the angle between the electron and the proton beam axis. Both electron and neutrino are assumed to be massless in this model. In the approximation that the boson spin is oriented along the $p\bar{p}$ axis the φ distribution of the decay is uniform.

The assumption that the W is polarized along the $p\bar{p}$ axis is only valid if the transverse momentum of the boson is zero. Corrections due to the finite boson p_{T} have been calculated by Mirkes [19] in the next to leading order QCD. In the Mirkes

[1]Addition of the central solenoid to the DØ detector in Run II of the Tevatron would allow one to use the muon channel for the W mass measurement along with the $W \to e\nu$ mode

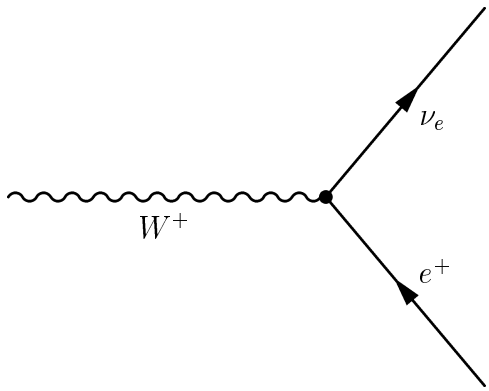

Figure 1.5: Lowest order diagram of the $W \to e\nu$ decay

model angular distribution 1.5 becomes

$$\mathcal{P}(\theta_{\mathrm{C-S}}) \propto 1 + \alpha_1 \cos\theta_{\mathrm{C-S}} + \alpha_2 \cos^2\theta_{\mathrm{C-S}}, \tag{1.6}$$

where $\theta_{\mathrm{C-S}}$ is the polar angle in the Collins–Soper frame [20].

Further details of the W and Z boson decay model will be given in Section 4.1.2.

Chapter 2

Experimental Apparatus

2.1 Fermilab Accelerator Complex

The Tevatron accelerator at the Fermi National Accelerator Laboratory is currently the highest energy collider in the world [21] with the center of mass energy of the proton and antiproton collisions of 1.8 TeV.

There are seven parts of the accelerator complex a particle has to go through to reach the collision point inside the DØ detector:

1. Cockroft–Walton accelerator (pre-accelerator),
2. Linear accelerator (Linac),
3. Booster synchrotron,
4. Main ring,

5. Antiproton source,

6. Antiproton debuncher,

7. Tevatron ring.

The Fermilab accelerator complex is shown in Fig. 2.1.

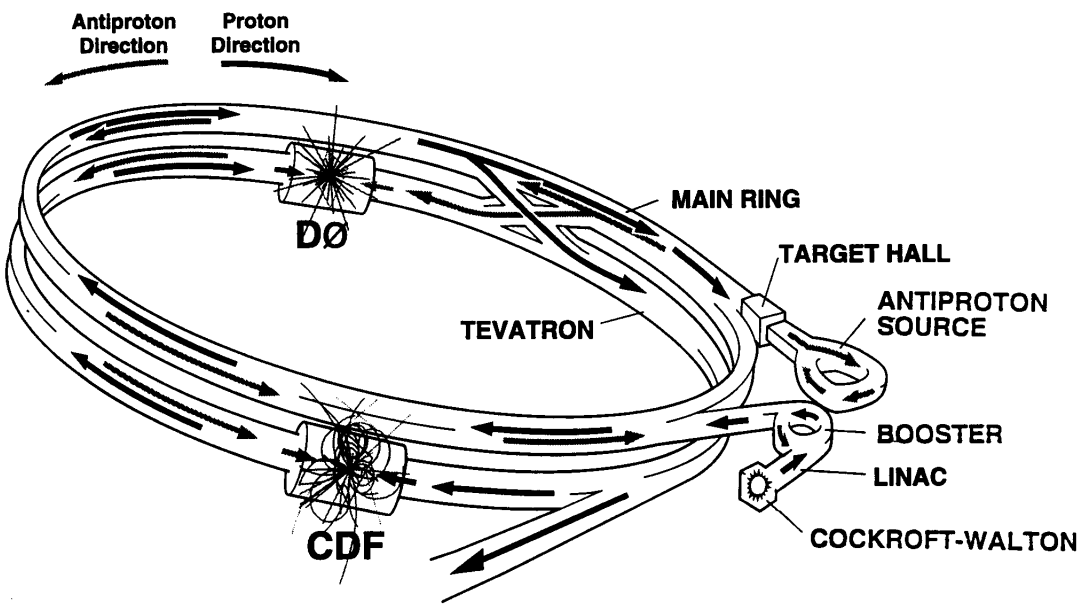

Figure 2.1: Fermilab accelerator complex

Protons originate from hydrogen gas interacting with a hot cesium cathode to produce H^- ions. The ions are accelerated by electric field in the Cockroft–Walton accelerator to an energy of 750 KeV and injected into the Linac where they are accelerated by the high radio frequency cavities to an energy of 200 MeV. The ions

then pass through a carbon foil which strips off the electrons thus creating a beam of protons.

The next stage of acceleration occurs in a 151 m diameter synchrotron called the booster. The synchrotron consists of three major parts: the radio frequency cavities, bending magnets, and focusing magnets. The alternating electric field in the cavities accelerates the bunches of particles every time they pass through the cavities and synchronize them with the cavity frequency. The dipole magnets are used to bend the orbit of the beam, and the alternate quadrupole magnets keep the beam focused in both transverse and longitudinal directions to ensure its stability and maintain high particle density. Protons travel about 20,000 orbits inside the booster as their energy is increased to 8 GeV. The booster repeats its cycle 12 times in rapid succession, delivering 12 pulses of bunches of protons for injection into the main ring.

The main ring is a proton synchrotron with a circumference of $\sim$6 km. It consists of a string of 774 conventional magnetic dipoles, 240 quadrupoles, and 18 radio frequency cavities. Once the protons have been injected into the main ring, they are accelerated to 150 GeV and then injected into the Tevatron ring. The main ring also produces a beam of 120 GeV protons which are extracted and used to generate antiprotons. The main ring beam pipe passes through the upper part of the DØ detector. Since proton losses can give rise to spurious signals in the detector, events are not recorded during the time of main ring activity.

For the antiproton production, the 120 GeV beam extracted from the main ring is directed onto a nickel or copper target. The collisions produce a large quantity of secondary particles including antiprotons which are selected by a series of magnets and transferred to the debuncher ring [1]. Here they are cooled and subsequently transferred to the accumulator ring for beam storage and further cooling.

The debuncher is designed to increase the density of antiprotons using two cooling techniques. The first one uses a computer coded radio frequency voltage to speed up slower protons and slow down the faster ones. The second technique, known as stochastic cooling, reduces the transverse momentum of the antiprotons: the particles deviated from the central orbit are detected by sensors, and signals are passed to kicker electrodes which correct the particle trajectories.

The Tevatron ring is located below the main ring in the same accelerator tunnel. It consists of 1000 superconducting magnets operating at the liquid helium temperature of $\simeq$4.6 K which allow acceleration of protons and antiprotons up to 900 GeV. The 150 GeV bunches of protons are transferred into the Tevatron from the main ring. The antiprotons are transferred from the accumulator ring to the main ring accelerated to 150 GeV, and then transferred to the Tevatron on the orbit in the opposite direction to the protons. During Run I, the Tevatron was operated with six proton and six antiproton bunches spaced by about 3.5 μs. The luminosity is increased by focusing

[1] At this point the beam is contaminated by negative pions, however, they are quickly damped because they have a significantly smaller mass

the beams with superconducting quadrupole magnets which are located near the interaction region. The beam spot has a transverse size of $\simeq 40\ \mu$m and a longitudinal size of about 30 cm. The proton and antiproton beams are allowed to collide at two points on the ring housing the DØ and CDF detectors. At the other four bunch crossing locations electrostatic separators keep the beams apart.

2.2 Overview of the DØ Detector. DØ Coordinate System

2.2.1 General Design and Purpose

The DØ detector [22] is a large general purpose detector (Fig. 2.2) designed to study processes with high transverse momentum and high mass states in $p\bar{p}$ collisions at the Tevatron collider. The detector has been collecting data since 1992. The main DØ physics topics are:

- Top quark analysis,
- Precision electroweak measurements,
- Perturbative QCD physics,
- B physics,
- Searches for physics beyond the Standard Model.

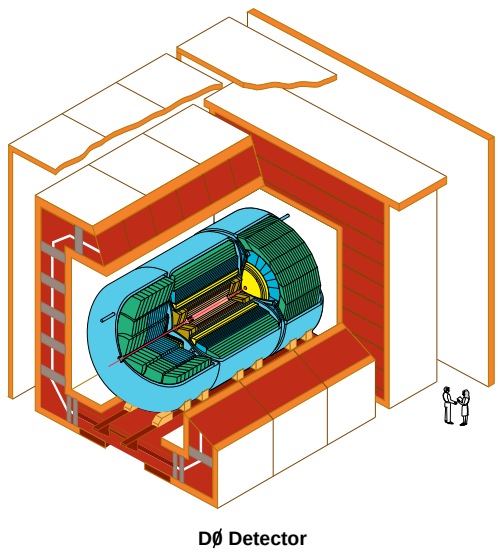

Figure 2.2: 3–D view of the DØ detector

The major components of the detector include the central tracking and transition radiation detectors, calorimeter, and the muon system. Fig. 2.3 shows the subsystems of the DØ detector.

2.2.2 DØ Coordinate System

DØ uses a right handed coordinate system with the z axis along the beam line, the positive direction coinciding with the direction of the proton beam (Fig. 2.4. The x axis is defined in the horizontal and the y axis — in the vertical direction. The azimuthal angle φ and the polar angle θ are defined in a standard way for the spherical coordinates: φ is measured with respect to the positive x direction, and θ — positive z direction.

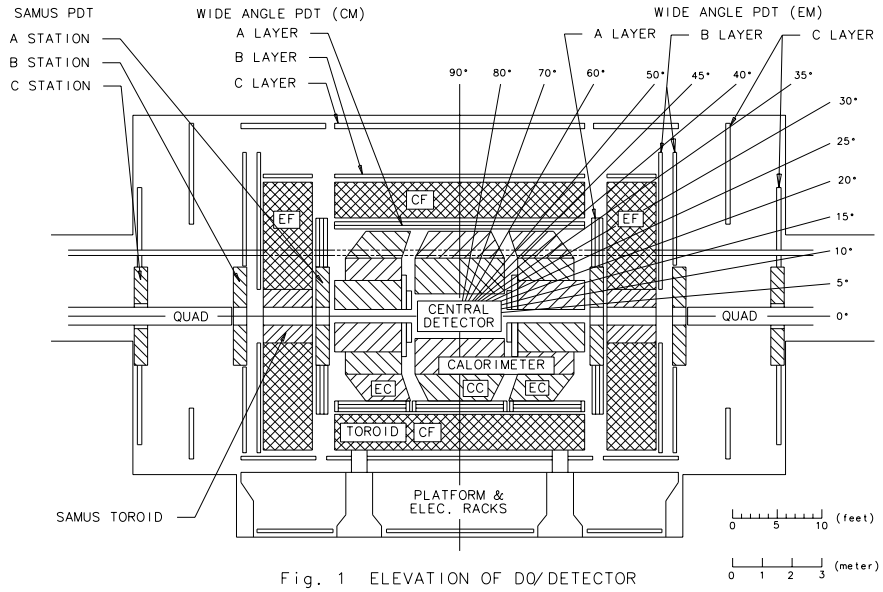

Figure 2.3: Side view of the DØ detector

It is convenient to introduce a function η of the polar angle θ called pseudorapidity:

$$\eta = -\ln \tan \frac{\theta}{2}. \tag{2.1}$$

In the high energy limit ($E \gg m$) η approaches the true rapidity y of the particle:

$$y = \frac{1}{2} \ln \left(\frac{E + p_z}{E - p_z} \right) \simeq \eta. \tag{2.2}$$

Rapidity is invariant under a longitudinal Lorenz boost, which makes it a useful variable.

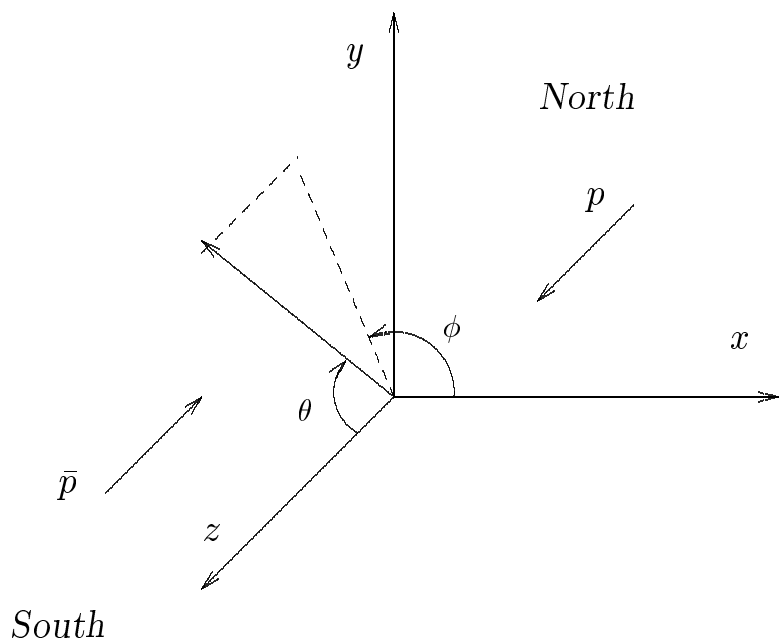

Figure 2.4: DØ coordinate system

It is important to distinguish between the "physics" (or "true") pseudorapidity and the detector η of a particle. The two are different because of the vertex z position spread of about 30 cm.

2.3 Central Detector

The central detector is designed to measure the trajectories of the charged particles originating from the interaction point and determine the interaction vertex position. It also provides additional information for particle identification. There is no magnetic

field in the central part of the DØ detector, therefore no particle momentum information is available from the central detector alone. The central detector is 270 cm long and 78 cm in radius. It provides good spatial resolution and energy loss determination in the region of $|\eta| < 3.2$.

The components of the central detector (see Fig. 2.5) are:

- Vertex drift chamber (VTX),
- Transition radiation detector (TRD),
- Central drift chamber (CDC),
- Two forward drift chambers (FDC).

2.3.1 Drift Chamber Operation Principle

A drift chamber consists of an enclosed volume filled with gas and arrays of anode and cathode wires creating regions of approximately uniform electric field. When a charged particle passes through the chamber, the electrons produced in the ionization are drawn to the anode wires and create a signal pulse on the wire. By measuring the time it takes to collect the charge, called the drift time, and the position of the hit wire, the particle coordinates can be determined.

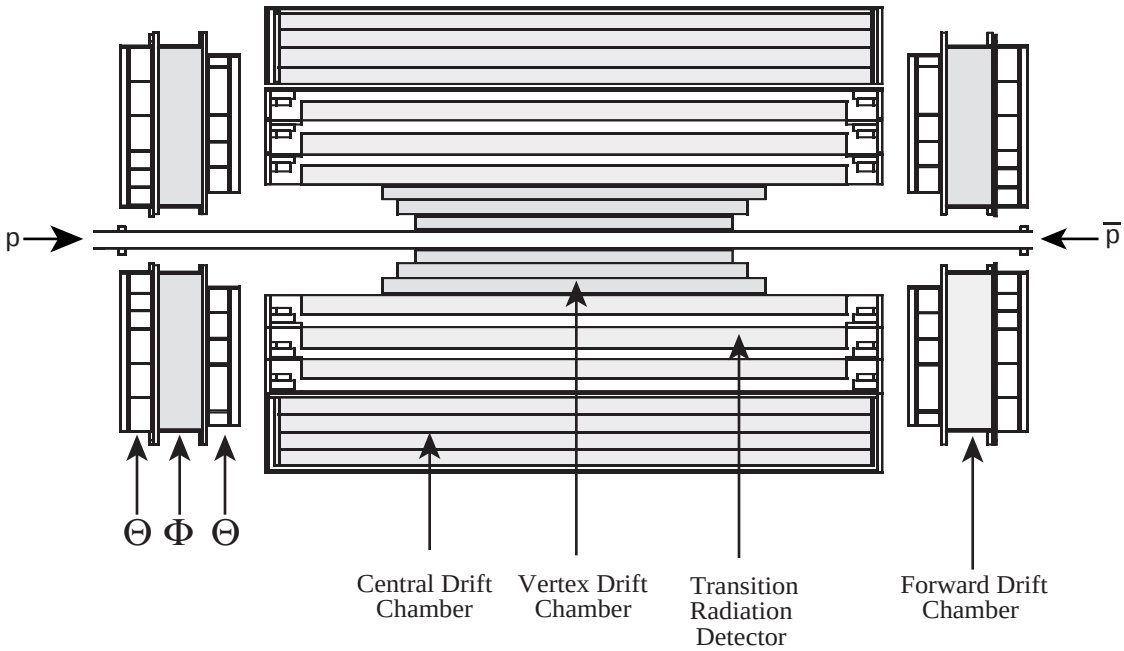

Figure 2.5: DØ central detector

2.3.2 Vertex Chamber (VTX)

The vertex chamber is the innermost part of the tracking detector with inner and outer radii of 3.7 cm and 16.2 cm, respectively. It consists of three layers of concentric cells with 110 cm long wires oriented parallel to the beam axis. The innermost layer has 16 cells in azimuth and the outer two layers have 32 cells each. The sense wires in each cell provide coordinate measurement in the (r, φ) plane. Signals from the wires are read out on both ends, which provides the z coordinate measurement. Figure 2.6 shows the (r, φ) view of the vertex chamber.

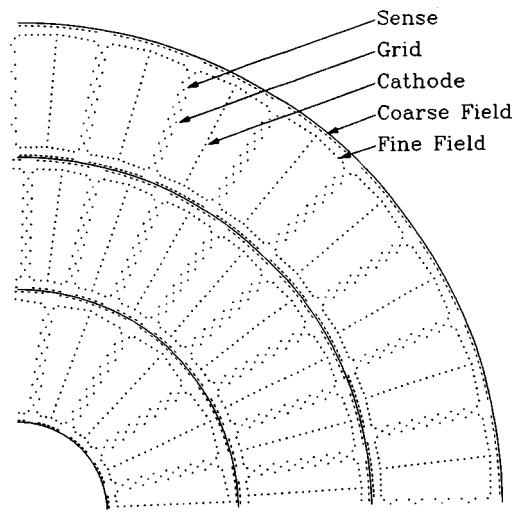

Figure 2.6: (r, φ) view of the vertex chamber

2.3.3 Transition Radiation Detector (TRD)

Operation principle of the TRD is based on the fact that highly relativistic particles ($\gamma > 10^3$) emit X-rays on a cone with the opening angle of $\sim 1/\gamma$ when they pass through a junction between two dielectric materials [23]. Thus, the energy flux of the radiation is proportional to the γ of the particle.

The DØ TRD information is used to distinguish electrons from charged pions independent of the calorimeter. The TRD consists of three separate modules, each containing a radiator and an X-ray detection chamber. The X-ray energy spectrum is determined by the thickness of the radiator layers and the gaps between these layers. Each of the modules contains 393 polypropylene foils with a mean gap of 150 μm located in a gaseous nitrogen volume. Proportional drift wire chambers are

used to convert the X-rays, and the resulting charge is radially drifted to sensor wires for readout. Both magnitude and the arrival time distribution of charge are used to distinguish electrons from hadrons. The DØ TRD is shown in Figure 2.7.

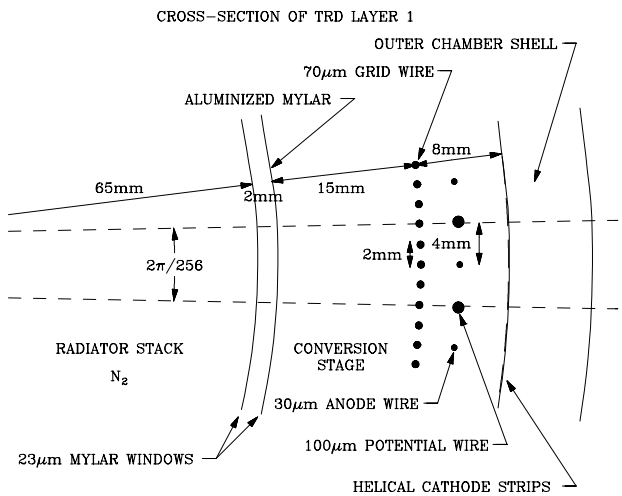

Figure 2.7: Transition radiation detector

2.3.4 Central Drift Chamber (CDC)

The central drift chamber is located between the TRD and the central calorimeter and is used to detect tracks at $|\eta| < 1.2$.

The CDC is a cylindrical shell of length 184 cm with a radial coverage from 49.5 cm to 74.5 cm. An end view of the CDC is shown in the Fig. 2.8. It consists of four concentric rings with 32 azimuthal cells per ring. Each cell contains 7 equally spaced tungsten sensor wires of 30 μm in diameter. The wires are parallel to the z axis and read out at one end to measure the φ coordinate. Delay lines embedded in

the inner and outer shelves of each cell are used to propagate the signals induced from the nearest neighboring anode wire. The z coordinate of a track is measured from the difference in the signal arrival times at the two ends. The position resolution in (r, φ) plane is $\simeq 180\,\mu$m and the z resolution is $\simeq 3\,$mm.

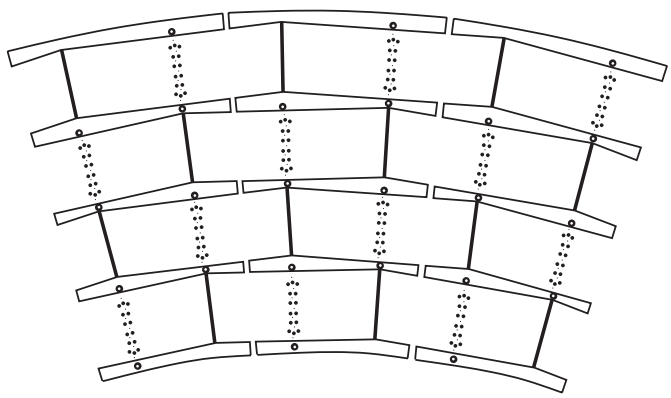

Figure 2.8: End view of the central drift chamber

2.3.5 Forward Drift Chambers (FDC)

The forward drift chambers are used to extend the coverage for charged particles up to $|\eta| < 3.1$. There are two FDC modules located at the either end of the central detector and just before the end cap calorimeters. Each FDC consists of a Φ chamber sandwiched between two Θ chambers, as shown in Fig. 2.9. The Φ module has radial sense wires and measures the φ coordinate and the Θ chambers measure the θ coordinate. The FDC position resolution is about $200\,\mu$m in the (r, φ) plane and $300\,\mu$m in (r, θ).

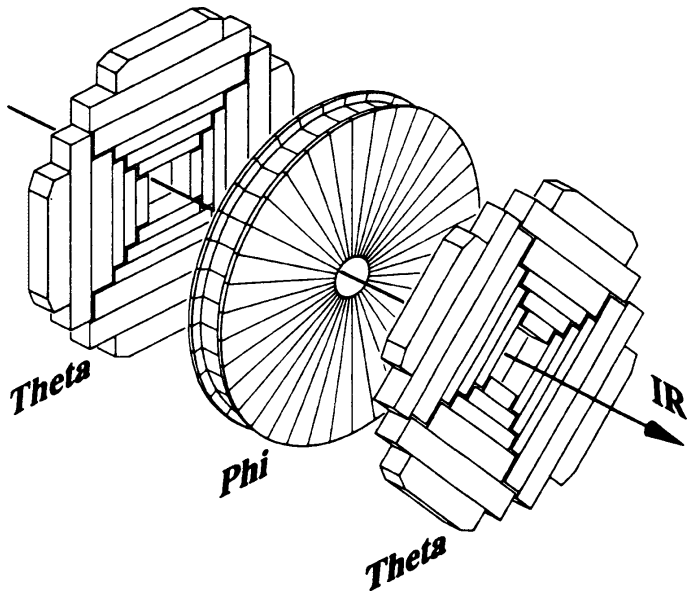

Figure 2.9: Forward drift chamber

2.4 Calorimeters

2.4.1 General Design and Operation Principle

Because of the absence of a central magnetic field that would enable a momentum measurement, the energy measurements at the DØ experiment rely heavily on the calorimeter. The calorimeter is also used for identification of electrons, photons, jets, and muons as well as determination of the transverse momentum balance in the event.

There are two types of particle showers in a calorimeter — electromagnetic and hadronic. An electro-magnetic shower consist of a cascade of electrons, positrons, and photons produced by bremsstrahlung and e^+e^- pair production. High energy elec-

trons or positrons radiate photons when passing through material, and the photons in turn create lower energy e^+e^- pairs. The number of particles increases exponentially until electrons reach the critical energy at which they lose the same amount of energy by radiation and ionization. After that, the number of particles decreases and their energies gradually dissipate through the process of ionization. Such an electromagnetic shower has a short and narrow energy profile. The longitudinal development of the showers is characterized by the radiation length X_0 of the calorimeter material, which is the the mean distance over which an electron loses all but $1/e$ of its energy by bremsstrahlung.

Hadronic showers are caused by the strong (nuclear) interactions between the hadrons and the nuclei of the calorimeter material. In such an interaction most of the energy is transferred to the nucleus resulting in the production of secondary hadrons, which in turn produce more hadrons. This cascade process terminates when the energies of the secondary hadrons are small enough to be exhausted by ionization or to be absorbed in a nuclear process. Hadronic showers tend to be wide and more penetrating than the electromagnetic showers [2]. A characteristic length of hadronic showers is the nuclear interaction length λ_I which is given approximately the following relation [24]:

$$\lambda_I = 35A^{1/3}\,\mathrm{g}\cdot\mathrm{cm}^{-2}, \tag{2.3}$$

[2] A hadronic showers also has an electromagnetic component produced by photons from the π^0 decays

where A is the atomic number of the material.

The DØ calorimeters consist of stacks of energy absorbing plates of depleted uranium, copper, or stainless steel and inter-plate gaps filled with liquid argon to sample the ionization produced by electromagnetic and hadronic showers. The calorimeter is divided into three parts: the Central Calorimeter (CC), the North End Calorimeter (ECN), and the South End Calorimeter (ECS). Each part is enclosed in a cryostat and has an electromagnetic section (EM) with 3 mm and 4 mm thick uranium plates in the central and forward region, respectively, a fine hadronic section with 6 mm uranium–niobium alloy plates and a coarse hadronic section with 46.5 mm either copper (CC) or stainless steel (EC) plates. A cut-away view of the DØ calorimeter is shown in Fig. 2.10.

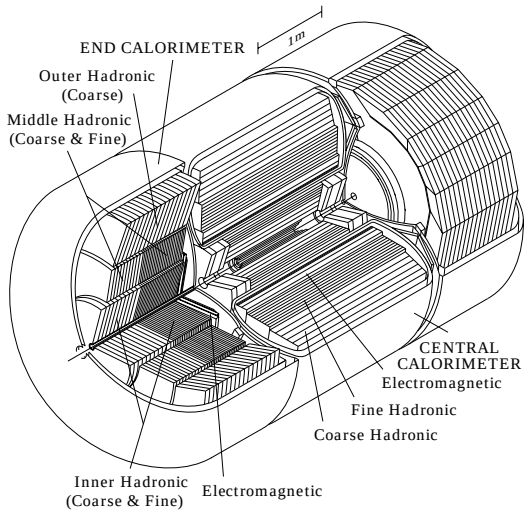

Figure 2.10: Cut-away view of the DØ calorimeter

The electromagnetic section of the calorimeter is $\simeq$21 radiation lengths deep and is divided into four longitudinal layers, EM_1 through EM_4, for the study of shower depth profiles. The hadronic sections are 7 to 9 nuclear interaction lengths thick. They are divided into four layers in the central calorimeter, three of which are called fine hadronic (FH_1 through FH_3) and one called coarse hadronic (CH). There is one coarse and four fine hadronic layers in the end calorimeter. The calorimeter segmentation in η and φ is 0.1×0.1 (see Fig. 2.4.1) except for 0.05×0.05 in the third EM layer, where the maximum of electromagnetic showers is expected.

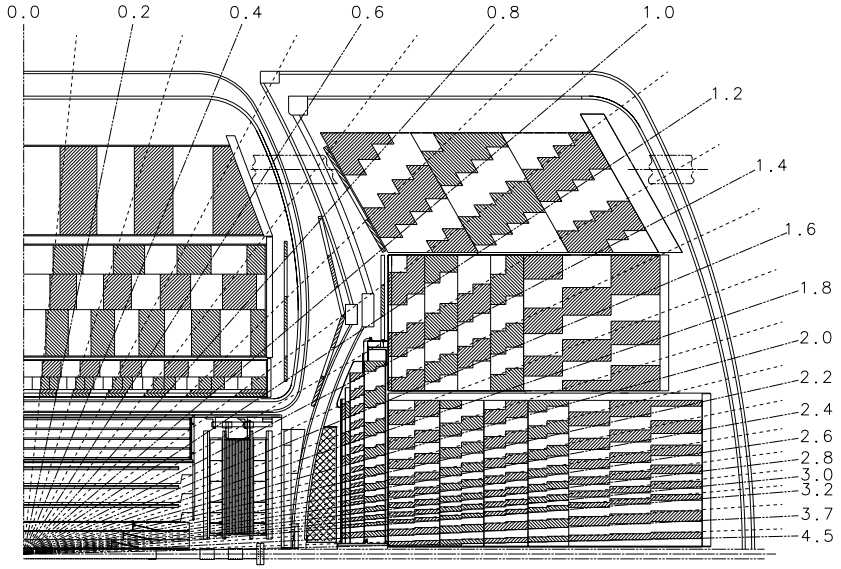

Figure 2.11: One quadrant of the calorimeter showing the arrangement of cells and towers

Fig. 2.12 shows a typical unit cell of the calorimeter modules. The absorber plate has a ground potential and the resistive surfaces of the readout are kept at +2000 V. The electron drift time across the gap is about 450 ns.

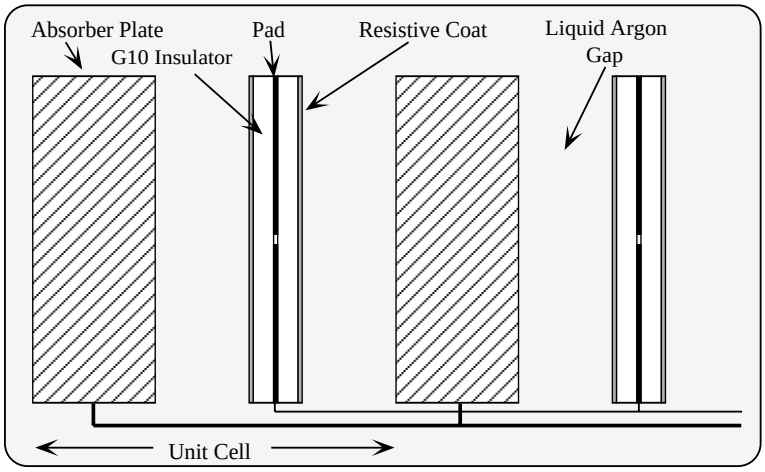

Figure 2.12: Calorimeter cell

2.4.2 Central Calorimeter

The central calorimeter consists of three concentric cylindrical shells 226 cm in length with a radial coverage of $75 < r < 222$ cm and a pseudorapidity coverage of approximately $|\eta| < 1$. There are 32 electromagnetic modules in the inner ring, 16 fine hadronic modules in the surrounding ring and 16 coarse hadronic modules in the outer ring.

2.4.3 End Calorimeters

There are two end calorimeters located at the north and south ends of the central calorimeter. Each calorimeter consists of one electromagnetic module, one inner hadronic module, and 16 middle and outer hadronic modules. The transverse segmentation of the electromagnetic module is identical to that in the central calorimeter except that the third layer segmentation 0.1×0.1 is for $|\eta| > 2.5$. The azimuthal boundaries of the middle and outer hadronic modules are offset to prevent projective cracks.

2.4.4 Inter-cryostat Detectors and Massless Gaps

There is a substantial amount of material in the form of cryostat walls which lies in the region of $0.8 \leq |\eta| \leq 1.4$. To provide uniform coverage across the gaps between the cryostats, two inter-cryostat detectors (ICD) are used. Each ICD consists of an array of scintillator tiles located between the CC and EC cryostats. The scintillation counters are used to correct for the energy deposited by the particles in the uninstrumented cryostat walls. Each ICD consists of 384 scintillator tiles of size 0.1×0.1 in η and φ, exactly matching the segmentation of the calorimeter cells.

In addition, separate readout cells called massless gaps are installed inside the CC and EC cryostats in the region of $0.8 \leq |\eta| \leq 1.4$. They consist of three liquid argon gaps and two readout boards with no absorber plates. The massless gap detectors

together with the ICD provide an approximation to the sampling of electromagnetic and hadronic showers with a worsened energy resolution.

2.4.5 Calorimeter Energy and Position Resolution

The performance of the calorimeter has been studied by using electron and pion beams with energies between 10 and 150 GeV at a test beam facility [25]. The energy resolution is parameterized as

$$\frac{\sigma}{E} = \sqrt{C^2 + \frac{S^2}{E} + \frac{N^2}{E^2}}, \tag{2.4}$$

where C, S, and N are called the constant, sampling, and noise term, respectively. Their values for electrons are found to be:

$$\begin{aligned} C &= 0.003 \pm 0.003, \\ S &= 0.157 \pm 0.006\,\sqrt{\mathrm{GeV}}, \\ N &= 0.29 \pm 0.03\,GeV. \end{aligned} \tag{2.5}$$

The position resolution of the calorimeter is important for identification of the electron backgrounds due to overlap of photons and charged particle tracks. This varies approximately as $1/\sqrt{E}$ and also varies between 0.8 and 1.2 mm over the full range of impact positions.

2.5 Muon System

2.5.1 General Design

The muon system (Fig. 2.13) is the outermost part of the DØ detector. It consists of five toroidal magnets surrounded by three layers of proportional drift tubes (PDT). The PDTs are arranged into the wide angle (WAMUS) and small angle (SAMUS) muon spectrometers. The toroids provide magnetic field of $\simeq 2\,\mathrm{T}$ to bend the muon trajectory measured by the drift chambers. This system enables muon identification and measurement of trajectories down to approximately 3 degrees from the beam line.

2.5.2 Wide Angle Muon Spectrometers (WAMUS)

Each WAMUS consists of a toroidal magnet and three layers of proportional drift tube planes. Layer A of PDT chambers is mounted on the inner surface of the magnetized toroids. Layers B and C are mounted outside of the toroids and are separated by $\simeq 1.4\,\mathrm{m}$. The A layer consists of four planes of PDT's whereas the B and C layers each have three planes. The central toroid covers the pseudorapidity region of $|\eta| \leq 1$ and two end toroids cover $1 < |\eta| \leq 2.5$.

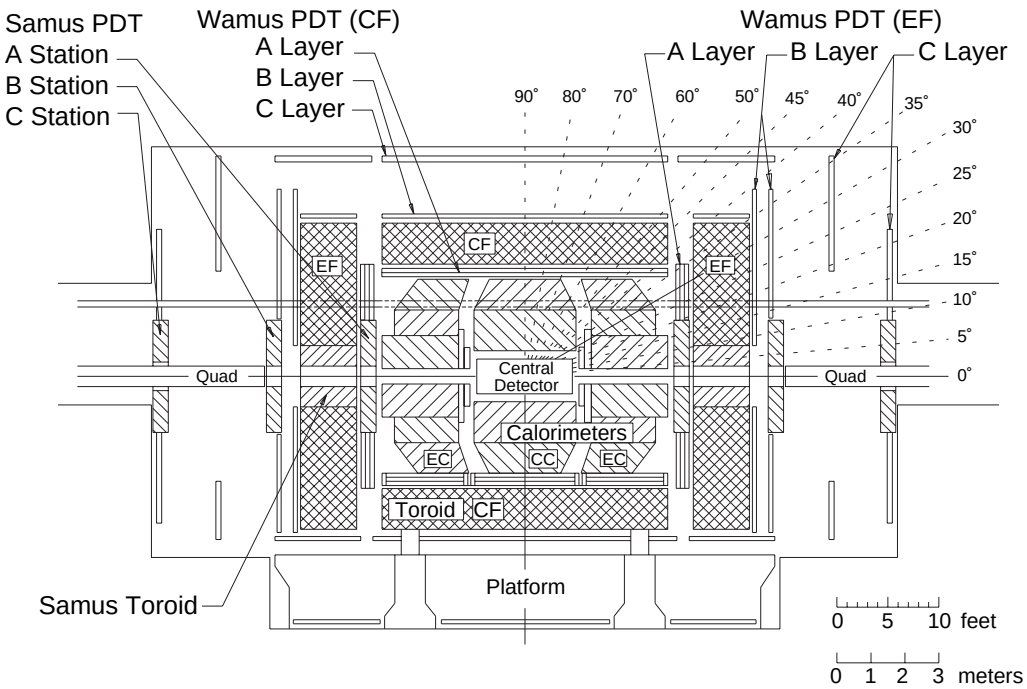

Figure 2.13: Muon system

2.5.3 Small Angle Muon Spectrometers (SAMUS)

The small angle muon spectrometers consist of two toroids and sets of PDT's. The chambers cover the pseudorapidity region of $2.5 \leq |\eta| \leq 3.5$ and are arranged into stations A, B, and C in a manner similar to the WAMUS spectrometers. Each layer consists of three doublets of proportional drift tubes oriented in x, y, and u directions, u being defined 45° with respect to the x and y axes.

2.6 Trigger and Data Acquisition

2.6.1 Trigger and Data Acquisition System Overview

The bunch crossing rate of the Tevatron during Run I (1992–1996) was 290 kHz. In order to select the interesting events at a rate of a few events per second from a large number of collisions, a four level trigger system is used in DØ. The first three levels of the trigger called Level 0, Level 1, and Level 1.5 are implemented in hardware, while the last stage called Level 2 is a software trigger.

Data from the detector subsystems and the L0 and L1 triggers are read out using eight high speed data cables. Events accepted by the L2 trigger are passed on to the host computer for run time monitoring and recording on tape. Events are buffered in the host until about 500 have been accumulated and then the file is closed and moved to a 8 mm data tape for permanent storage. The average size of the event is 500 Kbytes.

A block diagram of the DØ trigger and data acquisition system is shown in Fig. 2.6.1.

2.6.2 Level 0 (L0) Trigger

The Level 0 trigger indicates occurrences of inelastic collisions and serves as a luminosity monitor for the experiment. It consists of two arrays of scintillator hodoscopes

mounted between the forward drift chambers and the end calorimeters. The timing information from the L0 counters is used to determine the approximate z coordinate of the interaction for the subsequent trigger levels, and the hit rates are used to monitor instantaneous luminosity.

2.6.3 Level 1 (L1) and Level 1.5 (L1.5) Trigger

The L1 trigger collects information from the calorimeter and the muon system. It reduces the the input rate of $\sim 200\,\mathrm{kHz}$ from L0 down to $\sim 200\,\mathrm{Hz}$. The calorimeter trigger tower is a 0.2×0.2 region in the (η, φ) space up to $|\eta| < 4$ on which trigger decisions are based. The electromagnetic and fine hadronic energy for each tower is available for decision making. A number of global quantities are calculated and can be used further at the L1.5 and L2 triggers.

At Level 1.5 the two highest energy towers in η or φ are clustered together and two variables, the transverse EM energy and the EM fraction, are calculated for the new object:

$$E_{\mathrm{T}} = E_1(\mathrm{EM}) \sin\theta_1 + E_2(\mathrm{EM}) \sin\theta_2, \tag{2.6}$$

$$f_{\mathrm{EM}} = \frac{E_1(\mathrm{EM})}{E_1(\mathrm{EM}) + E_1(\mathrm{Had.})} + \frac{E_2(\mathrm{EM})}{E_2(\mathrm{EM}) + E_2(\mathrm{Had.})}, \tag{2.7}$$

where θ_i is the polar angle defined by the vertex and the center of the ith tower. The rate after the L1.5 trigger is reduced to about $100\,\mathrm{Hz}$.

2.6.4 Level 2 (L2) Trigger

The L2 trigger system is software based and consists of a farm of 50 parallel VAX nodes connected to the detector electronics and triggered by a set of eight 32-bit high speed (40 Mbytes/s) data cables. The L2 nodes are coordinated through the host computer. Event filtering is built around a series of filter tools with specific functions related to identification of a type of particle or event characteristic. These include tools for jets, muons, calorimeter EM clusters, track association with calorimeter clusters, $\sum E_{\mathrm{T}}$, and missing E_{T}. Other tools recognize specific noise or background conditions. The rate of events accepted at Level 2 is about 2 to 4 Hz.

2.6.5 Main Ring Veto Triggers

The main ring passes through the course hadronic portion of CC and EC calorimeters (see Section 2.1. It is active during the production of antiprotons and during injection of a new beam into the Tevatron. Beam loss from the main ring can cause spurious signals in the hadronic calorimeter and muon chambers. Typically this occurs once every 2.4 seconds when the protons are injected into the main ring and 300 ms later when the beam passes through transition. A timing circuit linked to the main ring control system is used to set a hardware flag. This is set every time the protons are injected and remains set for 400 ms until the beam has passed through transition and muon system recovers. In addition, smaller beam losses occur with every passage of

the beam. These are significant only if the passage of the main ring beam coincides with a $p\bar{p}$ crossing in the Tevatron. This is flagged using another bit which is set if a main ring beam passes within ± 800 ns of a crossing.

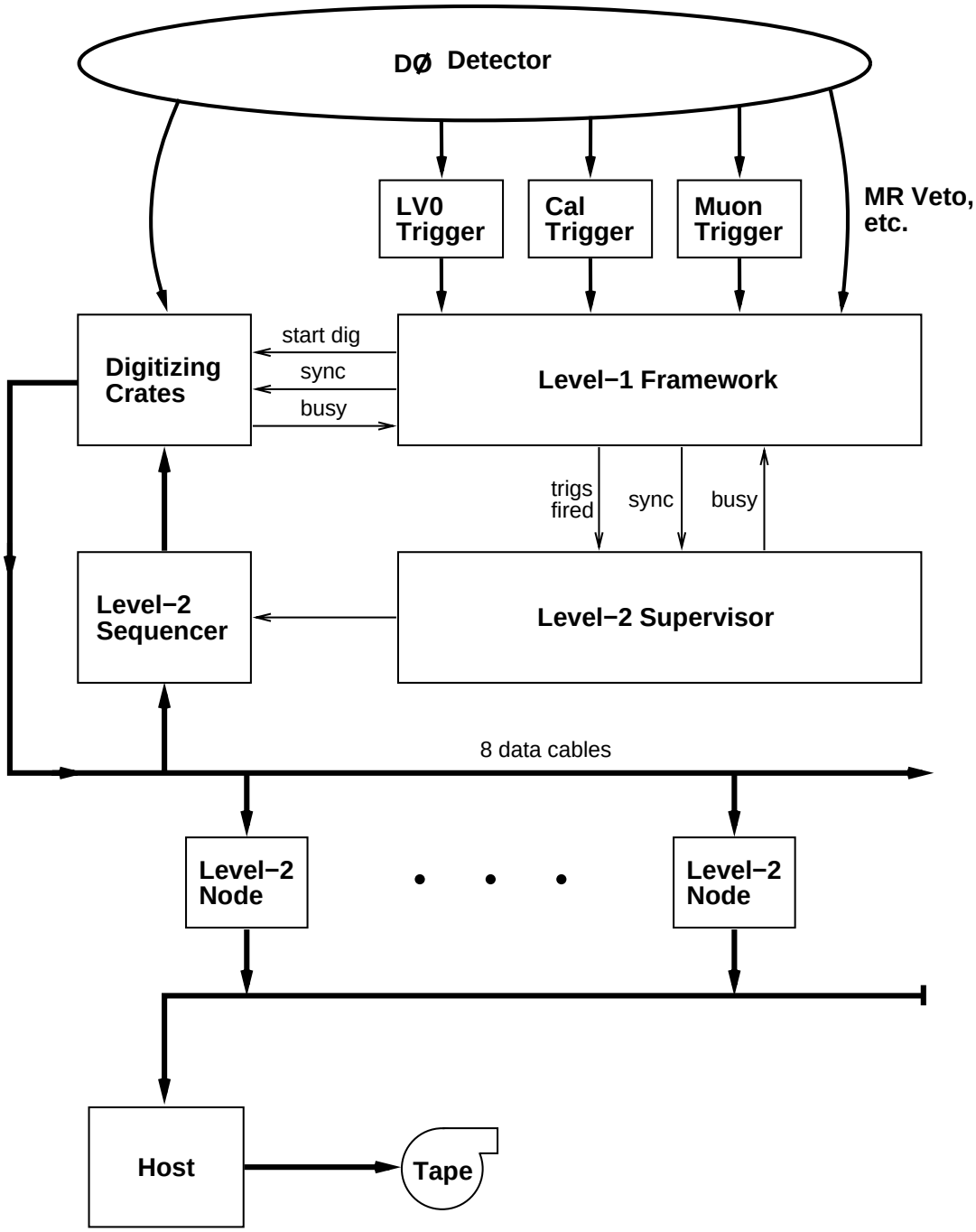

Figure 2.14: DØ trigger system

Chapter 3

Event Reconstruction and Particle Identification

3.1 DØRECO Program

The DØRECO package is a set of software algorithms which are used to perform particle and jet reconstruction. The reconstruction program is run on a farm of Silicon Graphics computers at the Fermilab central computing facility. In addition to the reconstruction of the data, DØRECO reduces the volume of the stored data by considerable fraction, thereby making data storage and handling easier. DØRECO creates three types of output data streams in the ZEBRA [26] format: Standard (STA), Data Summary Tape (DST) and Micro DST (μDST). The STA files are the largest in size and

contain all of the raw data plus the complete results of the reconstruction. The DST files are a compressed version of the STA files containing only processed information and the μDST files are the series of analysis specific highly compressed DST files.

3.2 Track Reconstruction and Vertex Finding

The track reconstruction procedure in the CDC, FDC, and vertex detector has the following three stages:

- Pulse identification and hit finding,
- Segment finding,
- Segment matching and global track fit.

First, the raw data containing the digitized charge *vs.* time for each wire address are unpacked. Individual pulses are identified by their leading and trailing edges, and each pulse is integrated to compute the total deposited charge. This is used later for calculating the dE/dx. After applying channel-to-channel calibration corrections, the time of arrival of the pulse is used to determine its position: the drift time to the sense wire determines the distance from the hit to the wire, and the arrival time from the delay lines gives the hit position along the wire.

Next, hits within single layers are connected. This process uses a road method in the (r, φ) plane. The z information is added to the segments afterwards. The road

is defined by a hit from the innermost wire and a hit from the outermost one. In the absence of the magnetic field all roads are straight. They are also constrained to be nearly radial since the tracks originate from the interaction vertex and do not encounter significant multiple scattering. The road width is chosen such that full efficiency is retained and the number of fake segments is minimized. The road width is about five times larger than the single hit resolution. All hits on the intermediate wires within the road are then considered. When a certain number of hits is found, a straight line fit is performed: a segment is identified if the χ^2 of the fit over the number of degrees of freedom is less than 10.

Once all segments are found they are linked into tracks. In order to be linked, two segments must be collinear: they have to point in the same direction in space, and their spatial mismatch must be small. Finally, a straight line fit is performed using all the hits from the linked segments: if the fit is good, and a minimum of three out of four layers are found, then a track is formed. Each track has five associated parameters: three coordinates of the center of gravity of the hits called the track centroid, the polar angle θ, and the azimuthal angle φ.

After the tracks have been identified, vertex positions can be reconstructed. In order to determine the z coordinate of the vertex (or vertices), each CDC track is projected onto the beam line. The vertex identified as the peak of the distribution of the z intercepts with the largest number of projected tracks is called primary. All

high p_{T} objects are assumed to originate from the primary vertex. Other vertices are associated with the minimum bias interactions in the event. The resolution of the vertex position with this method is about 2 cm. Multiple vertices are identified if they are separated by at least 7 cm.

3.3 Energy Measurement in the Calorimeter

The physical address of a calorimeter cell can be determined by a set of three integer indices: the η index $-37 \leq I_\eta \leq 37$, the φ index $1 \leq I_\varphi \leq 64$, and the layer (or depth) index $1 \leq I_{\mathrm{l}} \leq 17$. For the electromagnetic calorimeter, the layer index runs from 1 to 8, $I_{\mathrm{l}} = 1$ corresponding to the calorimeter section EM_1, $I_{\mathrm{l}} = 2$ to EM_2, $I_{\mathrm{l}} = 3$ through 6 to EM_3, $I_{\mathrm{l}} = 7$ to EM_4, and $I_{\mathrm{l}} = 8$ to FH_1.

Digitized ADC counts from the calorimeter cells are converted into energy through a set of calibration constants determined from the test beam data [25]. A cell is accepted for the cluster finding procedure if its energy passes a cell specific threshold. Vector

$$\vec{E}(I_\eta, I_\varphi, I_{\mathrm{l}}) = \hat{\vec{n}} E(I_\eta, I_\varphi, I_{\mathrm{l}}) \tag{3.1}$$

is defined for each cell, where $\hat{\vec{n}}$ is a unit vector defined by the interaction vertex and the center of the cell, and $E(I_\eta, I_\varphi, I_{\mathrm{l}})$ is the energy deposited in the cell. The

projection of vector 3.1 onto the transverse plane

$$E_{\mathrm{T}}(I_\eta, I_\varphi, I_{\mathrm{l}}) = E(I_\eta, I_\varphi, I_{\mathrm{l}}) \cos\theta \tag{3.2}$$

is called the transverse energy of the cell.

A collection of cells with specific I_η and I_φ is called a tower. Cell energies are combined into the electromagnetic and total tower energy as

$$E_{\mathrm{EM}}(I_\eta, I_\varphi) = \sum_{I_{\mathrm{l}}=1}^{8} E(I_\eta, I_\varphi, I_{\mathrm{l}}) \tag{3.3}$$

and

$$E_{\mathrm{total}}(I_\eta, I_\varphi) = \sum_{I_{\mathrm{l}}=1}^{17} E(I_\eta, I_\varphi, I_{\mathrm{l}}), \tag{3.4}$$

respectively. Components of vector 3.1 are combined into the corresponding tower energy components similar to 3.3 and 3.4, and the transverse energy ${E_{\mathrm{T}}}^{\mathrm{tower}}$ and the angular coordinates φ^{tower}, θ^{tower}, and η^{tower} are calculated.

3.4 Electron and Photon Reconstruction

3.4.1 Clustering Algorithm

Reconstruction of electron and photon energy uses a nearest neighbor cluster algorithm [27]. Starting with the highest transverse energy tower, the energy of adjacent

towers are added provided that they are above a few GeV E_{T} threshold, and that the cluster size is not too large. Each cluster is required to have at least 90% of its energy contained in the electromagnetic calorimeter, and at least 40% of the total energy contained in a single tower. The centroid of the cluster is then calculated using a logarithmic energy weighting technique to account for the transverse distribution of energy within the shower [28]. This gives a cluster position resolution of about 2 mm. At this point the reconstruction program searches for a central detector track pointing from the interaction vertex to the calorimeter cluster within a road of size ± 0.1 in both η and φ. If one or more tracks are found, the object is classified as an electron candidate. Otherwise, it is classified as a photon candidate.

The sample of electron candidates selected with the above procedure is contaminated with two types of background: the low energy charged hadrons overlapping with energetic photons from π^0 or η decays and the isolated photons converting to e^+e^- pairs in the beam pipe or tracking chambers. Several tools have been developed to suppress these backgrounds while retaining most of the real electrons for further analysis. These tools are discussed below.

3.4.2 Electromagnetic Energy Fraction and Isolation Fraction

The electromagnetic energy fraction of a cluster is the fraction of its energy contained in the electromagnetic calorimeter. For electrons or photons, the EM calorimeter contains almost all of the energy, while charged hadrons will deposit there only a small fraction of their energy. Thus the EM energy fraction of a cluster serves as a discriminant against charged hadrons.

Electromagnetic clusters are narrow as compared to the clusters produced by hadrons: they are usually contained in a cone of radius $R = 0.2$ in (η, phi) space, where the cone radius is defined as

$$R = \sqrt{(\Delta\eta)^2 + (\Delta\varphi)^2}. \tag{3.5}$$

DØ defines an isolation fraction f_{iso} as:

$$f_{\text{iso}} = \frac{E_{\text{total}}^{R=0.4} - E_{\text{EM}}^{\text{R}=0.2}}{E_{\text{EM}}^{R=0.2}}, \tag{3.6}$$

where $E_{\text{total}}^{R=0.4}$ is the total energy contained in the cone of radius 0.4 and $E_{\text{EM}}^{\text{R}=0.2}$ is the electromagnetic energy in a cone of radius 0.2. This gives a good measure to select isolated electrons.

3.4.3 Shower Shape — The Covariance Matrix

Electromagnetic showers can also be characterized by the fraction of the cluster energy deposited in each layer of the calorimeter. These amounts of energy are correlated and depend on the incident particle energy. The correlations can be used to distinguish electrons from hadrons and jets. Based on test beam studies and Monte Carlo simulations of electrons with energies between 10 and 150 GeV, a 41 variable covariance matrix is constructed [29]:

$$M_{ij} = \frac{1}{N} \sum_{n=1}^{N} (x_i^n - \bar{x}_i)(x_j^n - \bar{x}_j), \tag{3.7}$$

where N is the number of reference electrons, x_i^n is the ith variable of the nth electron, and $\bar{x}_i$ is the average of the ith variable over the N electrons. The 41 variables are:

- Fractional energies in EM_1, EM_2, and EM_4.
- Fractional energy in each cell of the 6×6 array of the EM_3 cells centered on the most energetic tower of the cluster.
- Logarithm of the cluster energy.
- z coordinate of the interaction vertex.

The H matrix is defined as the inverse of the covariance matrix 3.7. A χ^2 is computed for the observed shower shape:

$$\chi^2 = \sum_{i,j=1}^{41} (x_i - \bar{x}_i) H_{ij} (x_j - \bar{x}_j). \tag{3.8}$$

The lower the χ^2 is, the more the candidate cluster resembles an electron shower.

3.4.4 Ionization Energy Loss

Isolated photons that convert to e^+e^- pairs inside the beam pipe or the tracking chambers may result in tracks which match to EM clusters. Since there is no central magnetic field, the two tracks do not separate and are often too close to resolve. However, in the tracking chambers the ionization energy per unit length (dE/dx) of a e^+e^- pair is about twice that of a single charged particle.

3.4.5 Track Match Significance

A source of background for electrons is photons from the decay of π^0 or η mesons. The photons do not leave tracks in the central detector, but a track might appear if a charged particle is nearby. This background can be reduced by demanding a good spatial match between the calorimeter cluster and the nearby tracks. The track

match significance for the central region is defined as

$$\sigma_{\mathrm{trk}} = \sqrt{\left(\frac{\Delta\varphi}{\sigma_{\Delta\varphi}}\right)^2 + \left(\frac{\Delta z}{\sigma_{\Delta z}}\right)^2}, \tag{3.9}$$

where $\Delta\varphi$ and Δz are the azimuthal and longitudinal distances between the calorimeter cluster and the track, respectively and $\sigma_{\Delta\varphi}$ and $\sigma_{\Delta z}$ are the corresponding resolutions. In the forward region z is replaced by the radial distance r.

3.4.6 TRD Efficiency

The response of the Transition Radiation Detector (TRD) is characterized by the efficiency variable

$$\varepsilon(E) = \frac{\int_E^\infty \frac{\partial N}{\partial E'}(E')dE'}{\int_0^\infty \frac{\partial N}{\partial E'}(E')dE'}, \tag{3.10}$$

where E is the total energy recorded in the TRD minus that recorded in the layer with the largest signal and $\frac{\partial N}{\partial E'}$ is the energy spectrum from a sample of $W \to e\nu$ events. Since ε decreases as E increases, hadrons will tend to have values near unity while the distribution from electrons is roughly uniform over the allowed range of zero to one [30].

3.5 Missing Energy

Neutrinos and possibly other weakly interacting neutral particles are not directly observed in the event but their presence is inferred by momentum imbalance measured in the detector. A significant number of particles in the event have their momenta at a small angle with respect to the z axis and escape detection thus leaving a large uncertainty in the longitudinal momentum of the event. Therefore, only the transverse component of the missing momentum can be reconstructed.

The initial transverse momentum of a proton-antiproton system in collision is negligible, the final transverse momentum is expected to be small as well. Therefore, when a high p_{T} neutrino is produced, the negative sum transverse momenta of all the detected particles will match the transverse momentum of the neutrino. The quantity used to indicate the presence of a neutrino is called the missing transverse energy $\not{E}_{\mathrm{T}}$. It is defined so that it cancels the total transverse energy measured in the calorimeter:

$$\vec{\not{E}}_{\mathrm{T}} = -\sum_{I_\eta, I_\varphi, I_{\mathrm{l}}} \vec{E}_{\mathrm{T}}(I_\eta, I_\varphi, I_{\mathrm{l}}). \tag{3.11}$$

Since muons escape the calorimeter depositing only a small fraction of their energy, the apparent missing transverse energy defined in 3.11 must be corrected for the muon energy obtained from the muon system.

3.6 Jet Reconstruction

The most common algorithm used in DØ is the cone algorithm [31]. It is based on summing the observed calorimeter transverse energy within a fixed radius cone in the (η, φ) space.

Jet reconstruction starts from calculating the transverse energy for all of the calorimeter towers which are then sorted in order of decreasing E_{T}. Beginning with the highest E_{T} tower, clusters are formed by adding the towers within a radius R of the highest energy tower. The process is repeated for the remaining calorimeter towers and is referred to as preclustering. Next, the centroid of each cluster is calculated by performing an E_{T} weighted sum of the tower (η, φ) positions. Then the whole process is iterated using the jet centers as cluster seeds until the position of the cluster converges. This procedure is called cone clustering.

In order to remove any fake jets produced by calorimeter or main ring noise, DØ has developed a set of quality cuts based on the jet characteristics. These are cuts on the jet electromagnetic fraction (EMF) which is used to distinguish between EM objects (electrons and photons) and jets, the hot cell energy fraction (HCF) which helps reduce calorimeter noise, and the coarse hadronic energy fraction (CHF) which helps to remove activity caused by the main ring.

The measured jet energy usually is not equal to the energy of the original parton which formed the jet. There are several effects contributing to this and which are

corrected for using a DØ software algorithm `CAFIX` [32]. The corrections allow for the non-uniformities in the calorimeter and nonlinear response for low energy particles ($< 2\,\mathrm{GeV}$), electronics and the uranium absorber radioactivity noise, and the energy deposited in the jet cone from partons that do not come from the hard scattering process[1].

[1] These partons are typically from the soft interactions of spectator quarks and gluons within the proton and the antiproton and are referred to as the underlying event

Chapter 4

Analysis Procedure

4.1 A Fast W and Z Monte Carlo Generator

The transverse mass ratio method used in this analysis does not use Monte Carlo simulations to the extent the standard DØ W mass analysis method does. However, in order to substantiate the legitimacy of the ratio method as well as to study systematic effects on the W mass, various tests have been made using a fast Monte Carlo program called CMS (Columbia–Michigan State) [33, 34].

The simulation process in the CMS program is implemented as a sequence of the following three stages:

Vector boson production

At this stage the sign of the boson charge (for the W), the boson four-momentum,

the z coordinate of the vertex, and the event luminosity are generated.

Boson decay and final state radiation

The four-momenta of the boson decay products are calculated.

Detector smearing

A parameterized detector model is appied to calculate the observed electron momenta and the transverse recoil momentum.

4.1.1 Vector Boson Production Model

The theoretical model for the W and Z boson production in the CMS Monte Carlo is based on the assumption that the triple differential cross section can be factorized in the following manner:

$$\frac{d^3\sigma}{dydp_{\mathrm{T}}dm} \propto \frac{d^2\sigma}{dydp_{\mathrm{T}}} \cdot \frac{d\sigma}{dm}, \tag{4.1}$$

where m, p_{T}, and y are the mass, transverse momentum, and rapidity of the produced boson, respectively.

The resummed double differential cross section can be rewritten in terms of the Fourier transform:

$$\frac{d^2\sigma}{dp_{\mathrm{T}}dy} = \int \frac{d^2b}{(2\pi)^2} e^{ibp_{\mathrm{T}}} W(b), \tag{4.2}$$

where integration variable b has a meaning of the impact parameter in the transverse

plane. The low p_{T} (large b) region is handled by the following substitution [35]:

$$W(b) = W(b_*)e^{-S_{\mathrm{np}}(b)}, \tag{4.3}$$

where b_* is defined as

$$b_* = \frac{b}{\sqrt{1 + b^2/b_{\mathrm{max}}^2}}. \tag{4.4}$$

Factor $W(b_*)$ is a well defined (although complicated) function calculated in the perturbation theory [36]. Factor S_{np} incorporates the non-perturbative effects and has been calculated by Collins and Soper [37] and Arnold and Kauffman [38]. The CMS generator uses a more recent parameterization for S_{np} by Ladinsky and Yuan [39]:

$$S_{\mathrm{np}}(b) = g_1 b^2 + g_2 b^2 \ln \frac{Q}{2Q_0} + g_1 g_3 \ln(100 x_a x_b), \tag{4.5}$$

where Q is the mass of the boson, Q_0 is an arbitrary momentum scale, and x_a and x_b are the momentum fractions of the incoming quarks. Parameters g_1, g_2, and g_3 have been determined by Ladinsky and Yuan from the fit to the Drell–Yan and Z production data. For the choice of $Q_0 = 1.6\,\mathrm{GeV}$ and $b_{\mathrm{max}} = 0.5\,\mathrm{GeV}^{-1}$,

$$\begin{aligned} g_1 &= 0.11\ ^{+0.04}_{-0.03}\ \mathrm{GeV}^2, \\ g_2 &= 0.58\ ^{+0.1}_{-0.2}\ \mathrm{GeV}^2, \\ g_3 &= -1.5\ ^{+0.1}_{-0.1}\ \mathrm{GeV}^{-2}. \end{aligned} \tag{4.6}$$

A study of the relative contributions of each of the three g terms shows that g_2 is the dominant parameter [34].

The mass distribution is a product of the Breit–Wigner distribution by the parton luminosity term:

$$\frac{d\sigma}{dm} = \frac{m^2}{(m^2 - M^2)^2 + \dfrac{m^4\Gamma^4}{M^2}}\mathcal{L}_{\mathrm{p}}, \tag{4.7}$$

where M and Γ are the boson mass and width. For historical reasons, the parton luminosity is parameterized as

$$\mathcal{L}_{\mathrm{p}} = \frac{e^{-\beta m}}{m}. \tag{4.8}$$

Slope β is obtained from the parton distribution functions introduced in Equation 1.4 using the `HERWIG` Monte Carlo generator [40]. Figure 4.1.1 shows the parton luminosity effect on the mass distribution.

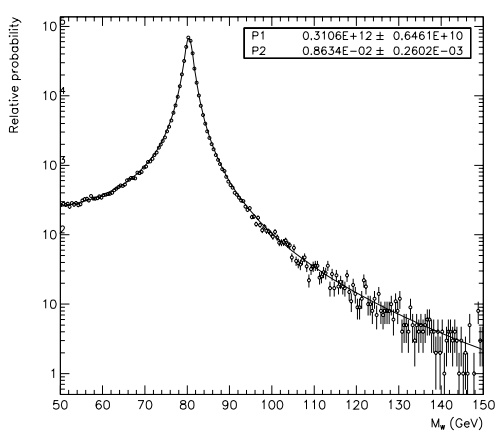

Figure 4.1: Mass distribution from `HERWIG` using the MRSA pdf showing the parton luminosity effect (plot from I. Adam [34])

The event vertex is picked up randomly from a Gaussian distribution with the mean and r.m.s. values obtained from the data.

4.1.2 Boson Decay

The angular distribution of the boson decay products is obtained using the Mirkes calculation introduced in Section 1.4.

There is an important correction to the decay process due to radiation of photons by the electron or by the W itself. The dominant effect relevant for the W mass measurement is the case when the final state electron emits a photon of significant energy at a large angle with respect to the electron so that it is not included into the electromagnetic cluster in the calorimeter. The final state radiation is simulated in the CMS Monte Carlo using the calculation by Berends and Kleiss [41].

There is an irreducible background to $W \to e\nu$ decays from the $W \to \tau\nu$ channel. The CMS generator simulates the latter in the same manner as the electron decay mode for a specified fraction of τ events with the subsequent τ decay into the electron and two neutrinos. The energy and angular distribution of the final state electron with respect to the τ momentum are selected from the two dimensional distribution obtained from the $\tau \to e\nu\nu$ decays simulated with the `ISAJET` Monte Carlo program [42].

4.1.3 Parameterized Detector Model

In order for the Monte Carlo program to be capable of generating millions of W and Z events at a reasonable CPU time expense, a parametric detector response model

has been used instead of full simulation of passage of particles through detector. Momenta of the decay products are smeared according to the electromagnetic and hadronic energy scale and resolution model which is described in detail in Chapter 5.

4.2 Overview of the Ratio Method

4.2.1 Kinematic Observables Used in the W Boson Mass Analysis

Since only the transverse component of the neutrino can be measured (see Section 3.5), the full invariant mass of the W boson cannot be reconstructed. Instead, the W mass analysis relies on other kinematic variables sensitive to the W boson mass. These variables are the electron and neutrino transverse momenta and a variable called the transverse mass [43]:

$$M_{\mathrm{T}} = \sqrt{2p_{\mathrm{T}}^{e}p_{\mathrm{T}}^{\nu}\left(1-\cos(\varphi^{e}-\varphi^{\nu})\right)}, \tag{4.9}$$

where p_{T}^{e} and p_{T}^{ν} are the transverse momenta of the electron and neutrino, respectively, and φ^{e} and φ^{ν} are the corresponding azimuthal angles. The transverse mass distribution has a Jacobian peak at the value of the mass of the parent particle and is smeared in the low mass region by the longitudinal components of the momenta of the particles.

Figure 4.2 shows the CMS Monte Carlo distributions of the transverse mass of

the W boson and transverse momentum of the electron. The transverse mass distribution is only weakly sensitive to the transverse momentum of the boson (*i.e.* on the boson production and decay model) but is affected considerably by the detector smearing. On the other hand, changes in the distribution of the electron transverse momentum due to the detector effects are insignificant but it is sensitive to the boson p_{T} distribution.

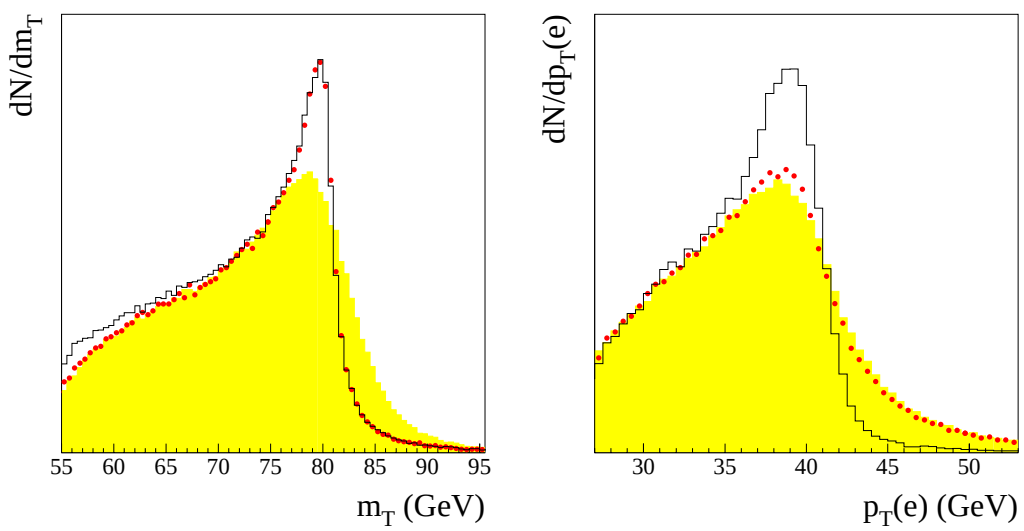

Figure 4.2: Distributions of the transverse mass of the W boson (left) and transverse momentum of the electron: solid histograms — $p_{\mathrm{T}}^{\mathrm{boson}} = 0$, dots — with correct $p_{\mathrm{T}}^{\mathrm{boson}}$ distribution, shaded area — with detector effects.

4.2.2 Ratio of Transverse Masses of the W and Z Bosons

In the standard DØ method of W boson mass measurement distributions of kinematic variables of the W decay products are compared to the corresponding Monte Carlo

templates for different input W masses [44]. The standard analysis uses a sample of Z events for detector calibration, tuning of Monte Carlo parameters, and cross checks.

In the ratio method [45] the transverse mass is reconstructed for each of the two data samples, $W \to e\nu$, and $Z \to e^+e^-$ with low transverse momentum of the boson [1]. If the M_{T} distribution of the Z sample is scaled down by a factor of $M(W)/M(Z)$, the new distribution would be identical to that of the W sample for ideally measured transverse momenta of the decay products. In Fig. 4.3 the transverse mass of the W boson is shown on top of the scaled transverse mass of the Z boson using the unsmeared (generator level) kinematic variables from the CMS Monte Carlo.

In this analysis, the W mass is obtained as a product of the Z mass value from the LEP collider at CERN by the scale factor that provides the best match between the two distributions corrected for the detector acceptance and energy resolution. The distributions are compared using a technique called the Kolmogorov–Smirnov test described in the next section.

A choice of the transverse mass over the transverse momentum of the electron or neutrino for the ratio fit was made because of a smaller sensitivity of m_{T} to the boson production physics (see Figure 4.2). The effect of the parton distribution functions is shown in Figure 4.4 for the three kinematic variables of the W decay products, m_{T}, p_{T}^{e}, and p_{T}^{ν}, for two choices of the parton distribution functions, CTEQ2M and

[1] The cut on the boson p_{T} reduces the difference between the two transverse mass distributions due to the production mechanism differences

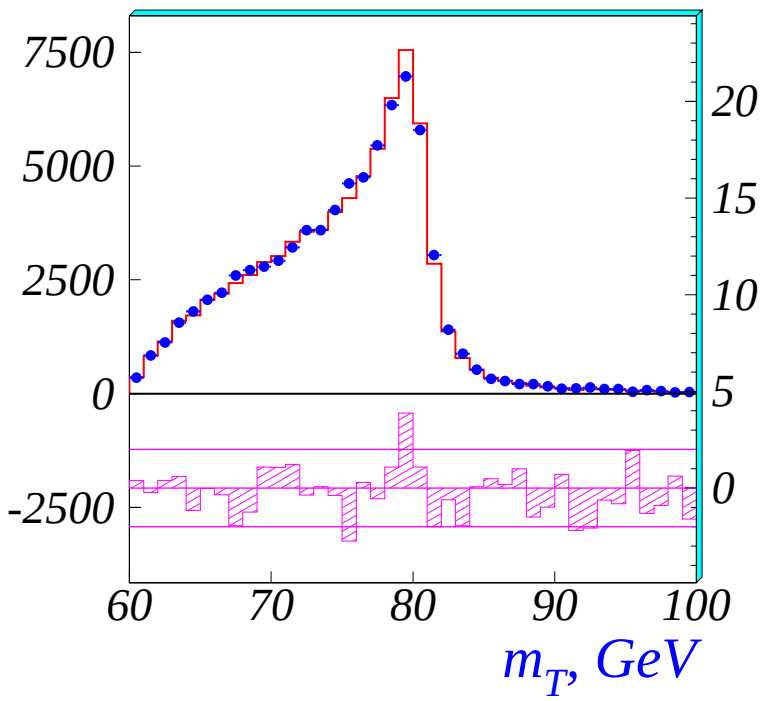

Figure 4.3: Transverse mass of the W boson (solid histogram) and scaled transverse mass of the Z boson (dots). Lower plot shows the bin-by-bin difference between the two distributions over the error with the horizontal band corresponding to the $\pm 2\sigma$ difference. This will be a standard convention further on. The disagreement between the two distributions at the peak is due to the production and decay effects.

MRSD$-'$. The difference between the spectra is slightly more pronounced for p_{T}^{e} and p_{T}^{ν} than for the transverse mass.

Another approach would be to use the difference instead of the ratio of the transverse masses. A disadvantage of this method is a larger sensitivity than in the ratio to the electron energy scale which cancels to the first order in the ratio. Dependence of the transverse mass ratio on various detector response parameters will be discussed

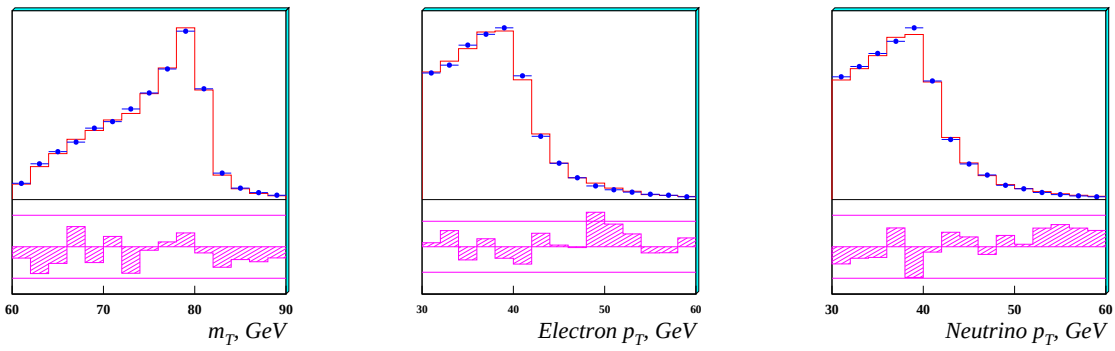

Figure 4.4: W transverse mass (left), electron p_{T} (center), and neutrino p_{T} W distributions for two choices of pdfs, CTEQ2M (solid line) and MRSD$-'$ (dots). The bottom part of each plot shows the bin by bin difference between the two spectra divided by the error, and the horizontal band corresponds to ± 2 standard deviations

in Section 6.3.2.

4.2.3 Kolmogorov–Smirnov Test

The Kolmogorov–Smirnov test is a statistical tool that provides a quantitative measure of the likelihood for two sets of measurements of a random variable to originate from a same parent distribution [46].

Let $x_1^{1,2} \leq x_2^{1,2} \leq \ldots \leq x_{m^{1,2}}^{1,2}$ be the two sets of measurements sorted in ascending order with weights $w_j^{1,2}$, $j = 1, \ldots m^{1,2}$. A single variable called the running difference

$$r = \sqrt{\frac{k^{(1)}k^{(2)}}{k^{(1)} + k^{(2)}}} \cdot \max_{\xi} |F^{(1)}(\xi) - F^{(2)}(\xi)| \tag{4.10}$$

is constructed from the two normalized cumulative distributions

$$F^{1,2}(\xi) = \frac{\sum_{l=1}^{p^{1,2}} w_l^{1,2}}{\sum_{l=1}^{m^{1,2}} w_l^{1,2}}, \tag{4.11}$$

where

$$k_i = \frac{\left(\sum_{j=1}^{m^{1,2}} w_j^{1,2}\right)^2}{\sum_{i=j}^{m^{1,2}} (w_j^{1,2})^2}, \tag{4.12}$$

and $x^{1,2}_{p^{1,2}} \leq \xi < x^{1,2}_{p^{1,2}+1}$. For sufficiently large numbers of events in distributions F^1 and F^2 picked randomly from the same parent distribution, probability p for the running difference defined by Equation 4.10 to be greater than a certain value ρ can be calculated as a function of ρ [47]. This probability will be referred to as the Kolmogorov–Smirnov probability. The dependence of $p(\rho)$ is shown in Fig. 4.2.3.

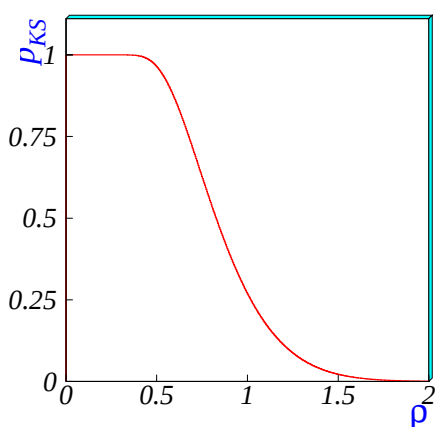

Figure 4.5: Kolmogorov–Smirnov probability as a function of the running difference between two distributions

Fig. 4.2.3 shows the Kolmogorov–Smirnov probability for the two transverse mass

distributions, $M_{\mathrm{T}}(W)$ and scaled $M_{\mathrm{T}}(Z)$ as a function of the scale factor for the unsmeared CMS variables. The maximum of this function corresponds to the best match between the two distributions shown in Fig. 4.3, and the width of the curve is interpreted as the statistical error of the W mass measurement. The $\sim 30\,\mathrm{MeV}$ difference between the position of the maximum of the Kolmogorov–Smirnov probability and the generated value of the W boson mass (80.4 GeV) is partially due to different production and decay mechanisms for the W and Z bosons. This effect will be discussed in Section 6.3 along with other systematic uncertainties.

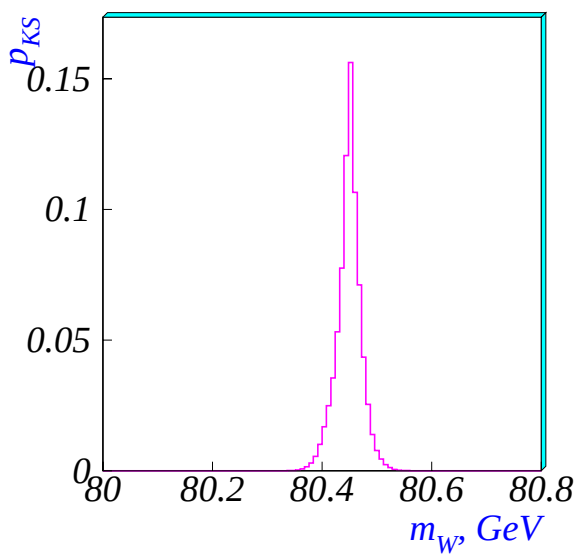

Figure 4.6: Kolmogorov–Smirnov probability for $M_{\mathrm{T}}(W)$ and scaled $M_{\mathrm{T}}(Z)$ as a function of the scale factor

Chapter 5

Understanding Detector Response

5.1 Energy Scale and Resolution

5.1.1 Electron Energy Scale

Data from the beam test of the calorimeter modules show a good linearity of the electron energy response of the calorimeter. Figure 5.1.1 shows the difference between the energy measured in the calorimeter, E, and the beam momentum, p, over the beam momentum, as a function of p [25].

In the collider environment, the calorimeter response in the transverse momentum range relevant for this analysis (20 to 70 GeV) can be parameterized as:

$$E = \alpha p + \beta, \tag{5.1}$$

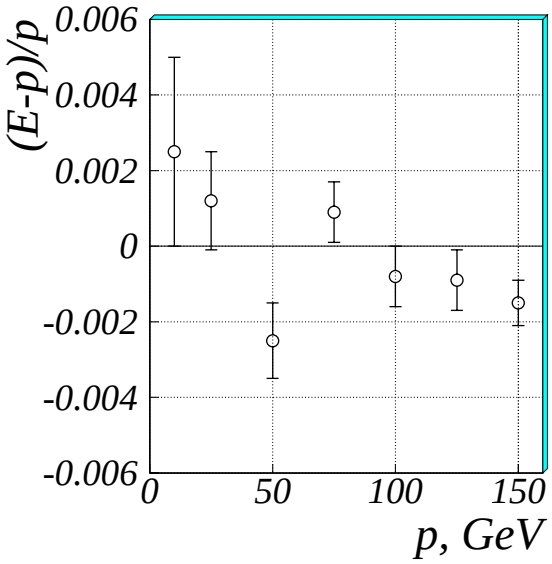

Figure 5.1: Difference between the energy measured in the calorimeter, E, and the beam momentum, p, over the beam momentum, as a function of p

where p is the true electron momentum and E is the energy measured by the calorimeter. Electron energy scale α and offset β have been obtained from the collider data using resonance decays $\pi^0 \to \gamma\gamma$, $J/\psi \to e^+e^-$, and $Z \to e^+e^-$ [49]. Table 5.1 summarizes the values of the electron energy scale for the central and forward calorimeters.

Parameter	Value
EM scale for the Central Calorimeter α_{CC}	0.9545
EM scale for the North End Calorimeter α_{ECN}	0.9525
EM scale for the South End Calorimeter α_{ECS}	0.9525

Table 5.1: Electron energy scale parameters

Measured transverse momentum of the electron, E_{T}^{e}, is related to the actual, p_{T}^{e},

in the following way:

$$E_{\mathrm{T}}^{e} = \alpha p_{\mathrm{T}}^{e} + \beta \sin\theta + U^{\mathrm{ue}} - U^{\mathrm{zs}}. \tag{5.2}$$

The U^{ue} term is the part of the hadronic energy in the event included in the electron cluster. It has been studied extensively in the standard DØ W mass analysis [49]. Figure 5.2 shows the momentum vectors in the transverse plane used in this analysis. Figure 5.3 shows the deviation from the nominal U^{ue} value in the central and forward

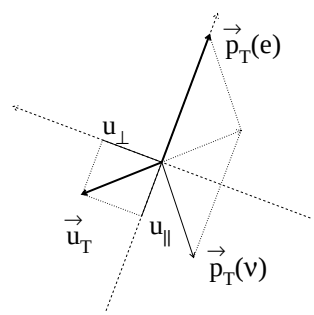

Figure 5.2: Momentum vectors in the transverse plane for the W event. $U_{\parallel}$ is the projection of the hadronic transverse momentum U_{T} onto the transverse direction of the electron

calorimeters. The U^{ue} distributions depend on the instantaneous luminosity of the event, $U_{\parallel}$ (projection of the hadronic transverse momentum onto the transverse direction of the electron shown in Figure 5.2), and angle θ of the electron. Dependence on the latter absorbs the $\beta \sin\theta$ term in Equation 5.2.

The zero suppression term U^{zs} is introduced due to the hadronic noise pedestal subtraction. Its value obtained from the full `GEANT` Monte Carlo simulation of the

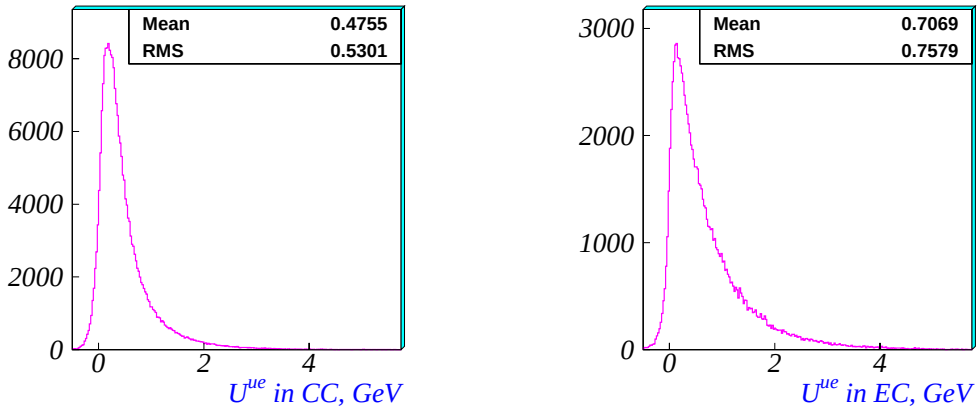

Figure 5.3: U^{ue} deviation from the nominal value in the central (left) and forward calorimeter

calorimeter is [49]:

$$U^{\mathrm{zs}} = 212 \pm 25\,\mathrm{MeV}. \tag{5.3}$$

It is found to be independent on η.

5.1.2 Electron Resolution

Electron energy resolution is parameterized according to Equation 2.4. The values of the resolution parameters were obtained from the fit to the Z collider data [34]. Table 5.2 shows the values of the electromagnetic resolution parameters.

To ensure good scaling of the transverse mass distribution, resolution of the Z and W electrons should be equal. Since the Z electrons on the average have higher p_{T} than the W and thus have better resolution, additional, "extra" resolution smearing

Parameter	Value
CC EM resolution sampling term S_{CC}	$0.130\,\mathrm{GeV}^{1/2}$
CC EM resolution constant term C_{CC}	0.0115
CC EM resolution noise term N_{CC}	0
North EC EM resolution sampling term S_{ECN}	$0.157\,\mathrm{GeV}^{1/2}$
North EC EM resolution constant term C_{ECN}	0.010
North EC EM resolution noise term N_{ECN}	0
South EC EM resolution sampling term S_{ECS}	$0.157\,\mathrm{GeV}^{1/2}$
South EC EM resolution constant term C_{ECS}	0.010
South EC EM resolution noise term N_{ECS}	0

Table 5.2: Electron energy resolution model parameters

is required for the Z electrons:

$$\left(\frac{\sigma}{< p_{\mathrm{T}}^{e} >}\right)_{Z}^{2} + \left(\frac{\sigma_{\mathrm{extra}}}{< p_{\mathrm{T}}^{e} >}\right)_{Z}^{2} = \left(\frac{\sigma}{< p_{\mathrm{T}}^{e} >}\right)_{W}^{2}. \tag{5.4}$$

5.1.3 Hadronic Energy Scale and Neutrino Energy

The following model for the hadronic response of the calorimeter is assumed in this analysis: the transverse momentum of the W is defined in terms of the transverse momenta of its decay products as

$$\vec{p}_{\mathrm{T}}^{W} = \vec{p}_{\mathrm{T}}^{\nu} + \vec{p}_{\mathrm{T}}^{e}, \tag{5.5}$$

and the total hadronic energy measured in the calorimeter is:

$$\vec{E}_{\mathrm{T}}^{\mathrm{hadr.}} = -\delta \cdot \vec{p}_{\mathrm{T}}^{W}. \tag{5.6}$$

This energy, $\vec{E}_{\mathrm{T}}^{\mathrm{hadr.}}$, is smeared with the detector resolution function, proportional to $\sqrt{\vec{E}_{\mathrm{T}}^{\mathrm{hadr.}}}$. Moreover, as discussed in Section 5.1.4, the model adds the resolution smearing effect from the remaining proton and antiproton "debris". This hadronic debris, the so-called underlying event, enters the calorimeter as well and resembles low transverse energy interactions — minimum bias events; events taken with an interaction trigger. Actual minimum bias events, taken at similar luminosity as the W events, are used to model the underlying event. Although the physics dictates minimum bias events to have zero net transverse momentum, detector resolution and imperfect calorimeter coverage build an apparent transverse energy $\vec{U}$ of several GeV on average. Randomly picked scaled $\vec{U}$ vectors picked from minimum bias data are added to $\vec{E}_{\mathrm{T}}^{\mathrm{hadr.}}$ to account for this additional smearing effect, but do not contribute to the mean value of $|\vec{E}_{\mathrm{T}}^{\mathrm{hadr.}}|$. The scale factor is tuned with $Z \to e^+e^-$ events.

The hadronic energy response was studied using the recoil distribution of the Z events [49], and the value of the scale factor δ was found to be

$$\delta = 0.693. \tag{5.7}$$

The measured transverse missing energy is equal to the negative of the sum of the hadronic energy and energy of the electron:

$$\vec{\not{E}}_{\mathrm{T}} = -\vec{E}_{\mathrm{T}}^{\mathrm{hadr.}} - \vec{E}_{\mathrm{T}}^{e}\left(1 - \frac{U^{\mathrm{ue}}}{E_{\mathrm{T}}^{e}}\right), \tag{5.8}$$

where the factor in parentheses prevents double counting the part of hadronic energy underlying the electron (the U^{ue} term is defined in Equation 5.2). Using Equation 5.6, the missing transverse energy becomes:

$$\vec{\not{E}}_{\mathrm{T}} = \delta \cdot \vec{p}_{\mathrm{T}}^{W} - \vec{E}_{\mathrm{T}}^{e}\left(1 - \frac{U^{\mathrm{ue}}}{E_{\mathrm{T}}^{e}}\right), \tag{5.9}$$

and the true transverse momentum of the neutrino:

$$\vec{p}_{\mathrm{T}}^{\nu} = \frac{\vec{\not{E}}_{\mathrm{T}}}{\delta} + \frac{\vec{E}_{\mathrm{T}}^{e}(1 - U^{\mathrm{ue}}/E_{\mathrm{T}}^{e})}{\delta} - \vec{p}_{\mathrm{T}}^{e}. \tag{5.10}$$

For the Z events $\vec{p}_{\mathrm{T}}^{\nu}$ in (5.5) becomes $\vec{p}_{\mathrm{T}}^{e_2}$, and a term associated with the second electron should be added to the left-hand side of (5.8). Thus the variable that matches $\vec{p}_{\mathrm{T}}^{\nu}$ in the transverse mass for the Z events is:

$$\vec{p}_{\mathrm{T}}^{e_2} = \frac{\vec{\not{E}}_{\mathrm{T}}}{\delta} + \frac{\vec{E}_{\mathrm{T}}^{e_1}(1 - U^{\mathrm{ue}}/E_{\mathrm{T}}^{e_1})}{\delta} - \vec{p}_{\mathrm{T}}^{e_1} + \frac{\vec{E}_{\mathrm{T}}^{e_2}(1 - U^{\mathrm{ue}}/E_{\mathrm{T}}^{e_2})}{\delta}. \tag{5.11}$$

5.1.4 Hadronic Energy Resolution

Similarly to the electron case, hadronic energy resolution should be the same for the W and Z events:

$$\left(\frac{\sigma}{< p_{\mathrm{T}} >}\right)^2_W = \left(\frac{\sigma}{< p_{\mathrm{T}} >}\right)^2_Z . \tag{5.12}$$

The boson momentum is assumed to scale with the mass, therefore additional smearing of the recoil and the hadronic energy underlying the electrons is necessary for the Z sample:

$$\sigma^{\mathrm{recoil}}_{\mathrm{extra}} = \sigma^{\mathrm{recoil}}(W)\sqrt{\left(\frac{M_Z}{M_W}\right)^2 - 1}, \tag{5.13}$$

$$\sigma^{\mathrm{ue}}_{\mathrm{extra}} = \sigma^{\mathrm{ue}}(W)\sqrt{\left(\frac{M_Z}{M_W}\right)^2 - 1}. \tag{5.14}$$

As in the conventional DØ W mass analysis, the hadronic resolution is parameterized separately for the hard and soft component of the recoil. The hard component of the recoil is parameterized as [44]:

$$\sigma_{\mathrm{hard}} = s\sqrt{E_{\mathrm{T}}^{\mathrm{hadr.}}}, \tag{5.15}$$

with the value of factor s:

$$s = (0.49 \pm 0.14)\sqrt{\mathrm{GeV}}. \tag{5.16}$$

The soft component of the recoil is modeled by the minimum bias data. It depends on the instantaneous luminosity of the event and has been examined in the standard W boson mass analysis [49]. Fig. 5.4 shows the minimum bias transverse momentum distribution for two intervals of the instantaneous luminosity values.

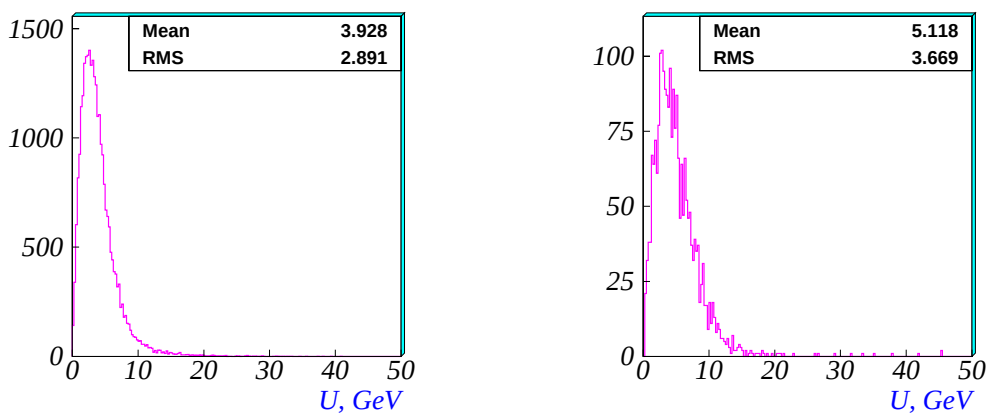

Figure 5.4: Minimum bias transverse momentum distribution. Left — for the instantaneous luminosity range from 0 to $10^{30}\,\mathrm{cm}^{-2}\mathrm{s}^{-1}$, right — from $1.6 \cdot 10^{31}\,\mathrm{cm}^{-2}\mathrm{s}^{-1}$ to $2.5 \cdot 10^{31}\,\mathrm{cm}^{-2}\mathrm{s}^{-1}$

5.1.5 Procedure for Applying Energy Response and Resolution Corrections

When calculating the true electron transverse momentum, a value for the U^{ue} term is picked up from the distribution corrected for $U_{||}$ and luminosity (Fig. 5.3).

Additional — "extra" smearing of the electron and the hard component of the recoil momentum of the Z events is picked up randomly from the Gaussian distri-

bution with the zero mean value and the corresponding σ using parameters from either Table 5.2 or Equations 5.15 and 5.16. A similar procedure applies for the soft hadronic component: the magnitude of the momentum correction is picked up from a distribution corresponding to the given luminosity interval, and the azimuthal angle is picked up from the uniform distribution in the range from 0 to 2π.

In order to average over these random corrections, they are applied repeatedly to the original W and Z samples until the average stabilizes (usually ~ 50 times). The final W mass is calculated as the average over the values obtained from the Kolmogorov–Smirnov test in each of these smearing iterations.

5.2 Event Selection Efficiency

Different event selection efficiencies for the W and Z samples would bias the Kolmogorov–Smirnov test output value. To correct for that effect, weights are applied to both W and Z events depending on the event topology. The weights are calculated as the inverse of the selection efficiencies for a given topology. The efficiencies were measured in the W and Z production cross section analysis [48]. The values of the efficiency are summarized in table 5.3.

Event type	Selection efficiency
W, central electron	0.731±0.018
W, forward electron	0.684±0.028
Z, two central electrons	0.753±0.020
Z, one central and one forward electron	0.748±0.023
Z, two forward electrons	0.742±0.042

Table 5.3: W and Z event selection efficiencies

In order for these efficiencies to be applicable in this analysis, event selection cuts are kept the same as in the cross section analysis.

5.3 Detector Acceptance Effects on the Mass Ratio

W and Z event selection cuts described in Section 6.1.3 require the W electron and both Z electrons to be outside the regions of the calorimeter where electron identification is poor. However, this requirement cannot be applied to the W neutrino. This section describes a procedure that allows to correct for this acceptance difference for the two samples.

5.3.1 η Dependent Weight

This correction compensates for the difference in the allowed η regions for the W and Z events. For each W event edges of the calorimeter gaps are projected onto the beam axis at angle θ of the electron. The distribution of the interaction vertex normalized to unity is integrated over those projected intervals not shadowed by the calorimeter boundaries, giving the probability for the event to be detected by the calorimeter (Fig. 5.5).

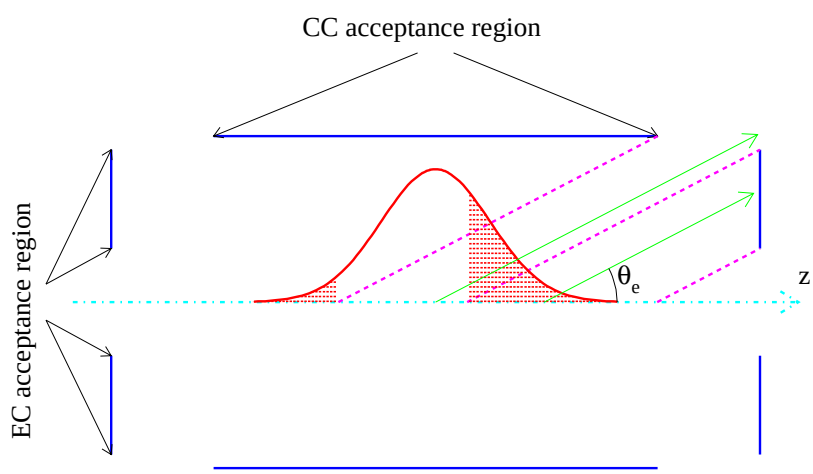

Figure 5.5: Calculation of probability for a single electron (W) event to be detected by the calorimeter. The Gaussian represents the experimental vertex distribution, the dashed lines show the projections of the CC and EC boundaries onto the z axis at angle θ of the electron. The event is detected if the vertex position is within the shaded region.

The event is assigned a weight equal to the inverse of the detection probability thus compensating the distributions for undetected events with the same θ of the electron. For the Z events the probability is calculated similarly with the integration region obtained as the intersection of the projection intervals for the two electrons. Fig. 5.6 shows the event detection probability as a function of η of the electron for the W events and as a function of pseudorapidities of the two electrons for the Z events. One can see that the detection probability never turns zero within the η region of interest so the weight can always be calculated.

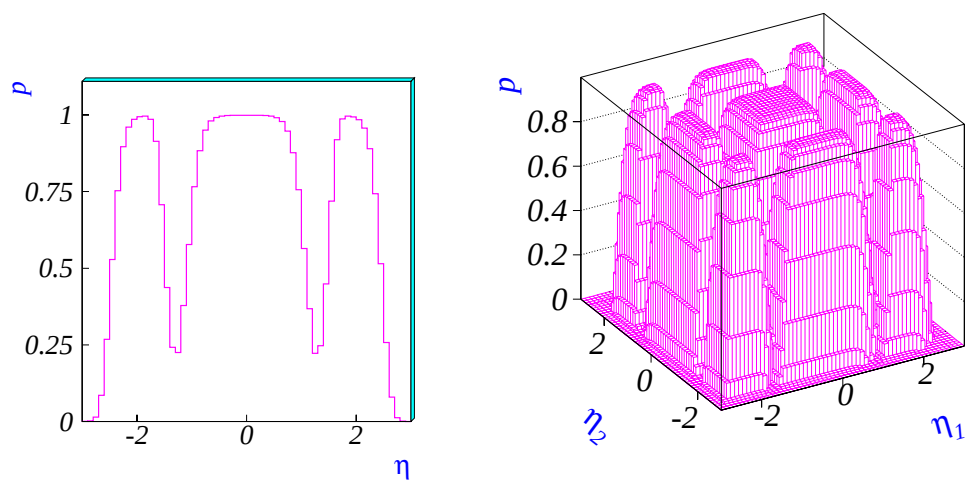

Figure 5.6: Event detection probability: left — as a function of the electron η for the W events, right — as a function of pseudorapidities of the two electrons for the Z events

The effect of this procedure is illustrated in Fig. 5.7 showing the loose electron

pseudorapidity distributions and the Kolmogorov–Smirnov probability *vs.* the W mass. The gaps in the η distribution due to the fiducial cuts are closed, and the output value of the Kolmogorov–Smirnov test moved closer to the generated value after the weights have been applied.

No fiducial cuts:

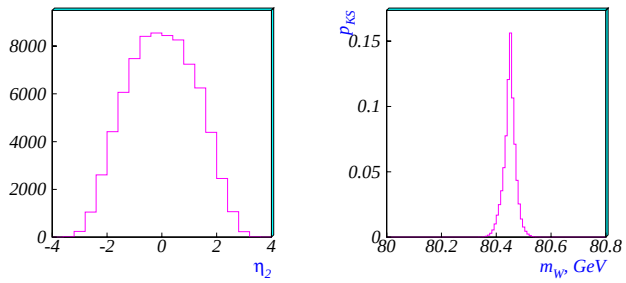

$$M_W = 80.45\,\text{GeV}$$

$$\text{r.m.s.} = 0.05\,\text{GeV}$$

Cuts applied, no weights:

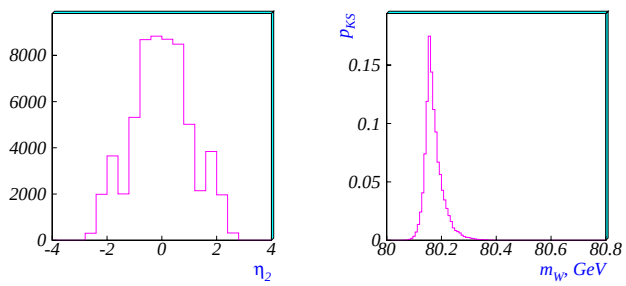

$$M_W = 80.17\,\text{GeV}$$

$$\text{r.m.s.} = 0.04\,\text{GeV}$$

Both cuts and weights applied:

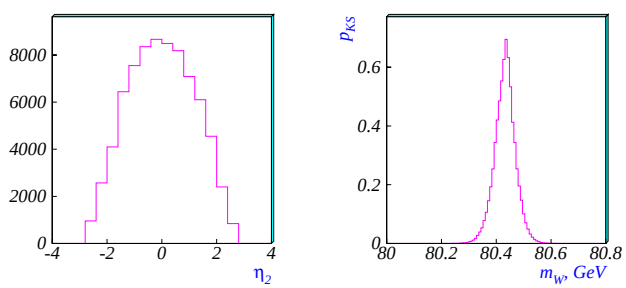

$$M_W = 80.43\,\text{GeV}$$

$$\text{r.m.s.} = 0.05\,\text{GeV}$$

Figure 5.7: Pseudorapidity distributions of the second Z electron (left plots) and Kolmogorov–Smirnov probability as a function of the W mass with and without fiducial cuts and acceptance weights

5.3.2 φ Dependent Weight

Electrons in the central calorimeter are required to be away from the calorimeter module boundaries (see Section 6.1.3). This cut introduces an acceptance difference between the W and Z events with different topologies of the final state which is corrected for by applying a weight equal to the inverse probability for the event to be inside the acceptable φ region.

5.4 Monte Carlo Tests

The analysis procedure described above has been tested on the CMS Monte Carlo W and Z samples containing about 700,000 and 300,000 events, respectively, using the MRSA parton distribution functions. The transverse mass distributions used in the Kolmogorov–Smirnov fit are shown in Fig. 5.4. Fig. 5.10 shows the transverse momenta of the decay products. Fig. 5.4 shows the transverse momentum of the boson.

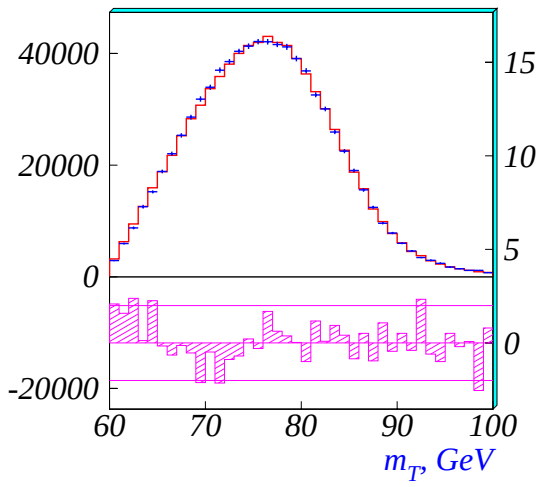

Figure 5.8: Transverse mass of the W boson (solid) and scaled transverse mass of the Z boson (dots). The scale factor here and on the other plots corresponds to the maximum Kolmogorov–Smirnov probability

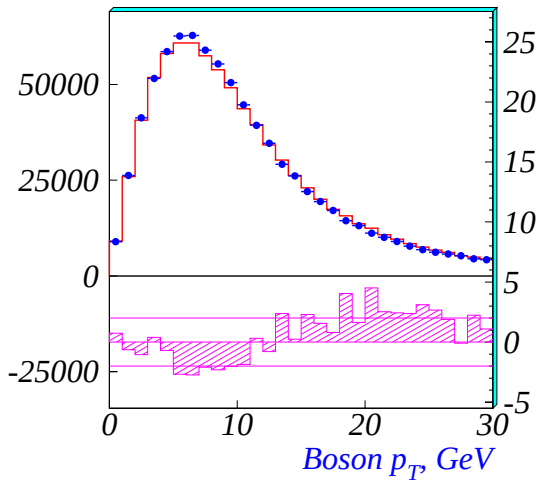

Figure 5.9: p_{T} of the boson. The discrepancy between the two distributions at high p_{T} values is due to the different masses and production mechanisms of the two bosons (different parton distributions of u and v quarks).

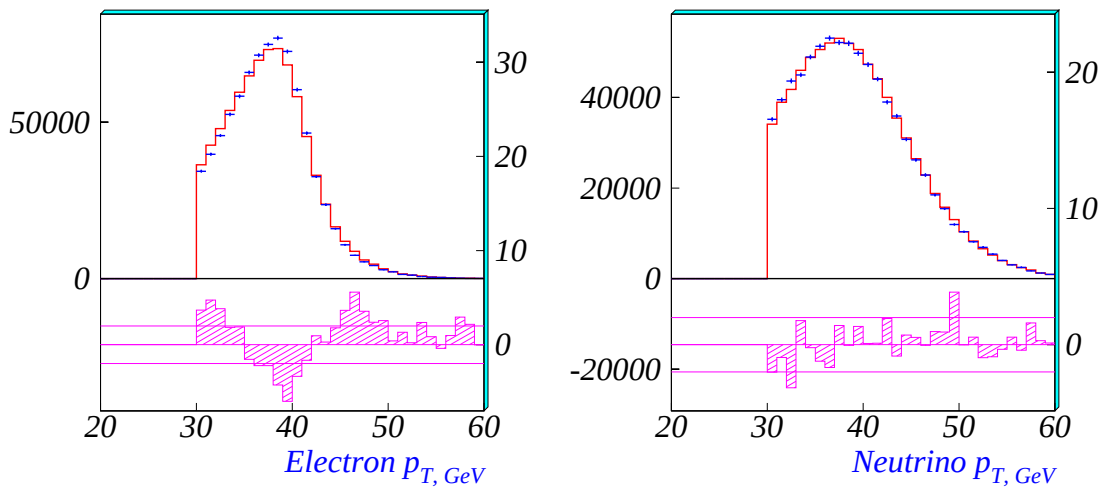

Figure 5.10: Left — p_{T} of the electron (scaled for the Z), right — p_{T} of the W neutrino on top of the scaled p_{T} of the second Z electron. Solid line — W, points — Z

The effects of the weighting procedure on the angular distributions of the W and Z electrons are shown in Fig. 5.4. The two distributions are different because of the different decay model and boson η distributions of the W and Z.

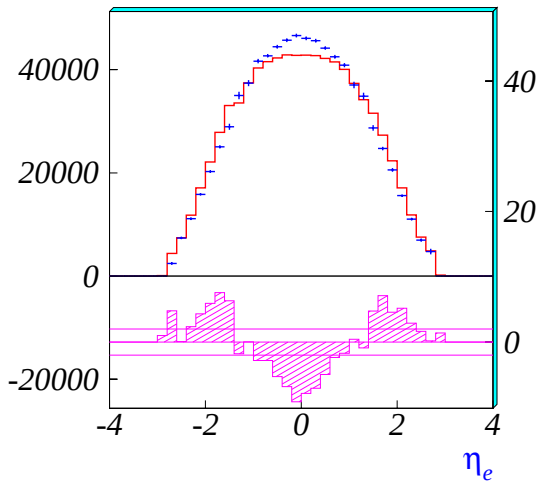

Figure 5.11: Pseudorapidity of the W and Z electrons

In order to remove a bias due to the extra smearing of the Z sample, the Kolmogorov–Smirnov test was performed 100 times for different random values of the added smearing corrections. Each such smearing iteration produced a Kolmogorov–Smirnov probability as a function of the W mass. These functions are shown in Fig. 5.4. The maximum of the Kolmogorov–Smirnov probability and the width of the probability curve for 100 smearing iterations are plotted in Fig. 5.13. The mean values of the two distributions are interpreted as the output W mass and the statistical error, respectively. The output value of the mass is therefore $M_{\text{out}}(W) = 80.384 \pm 0.045\,\text{GeV}$ for the generator input of $80.4\,\text{GeV}$[1].

[1]For very large samples ($\sim 10^7$ W events) the mean value of the width distribution and the r.m.s. of the distribution of mean values approach the same limit. For samples of limited size ($\sim 10^5$ events) the mean of the width distribution is taken for the statistical error. For limited size samples this choice for uncertainty turns out to be the same as the result from an ensemble test (see Section 6.2). However, the fact that the two values are different for limited size samples is not yet understood and needs to be investigated in the future.

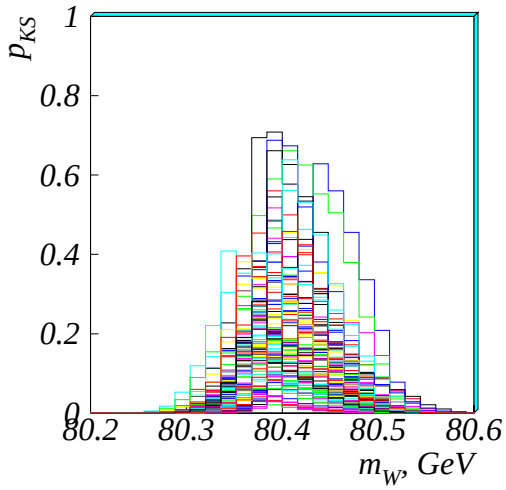

Figure 5.12: Kolmogorov–Smirnov probability as a function of the W mass for 100 Z extra smearing iterations

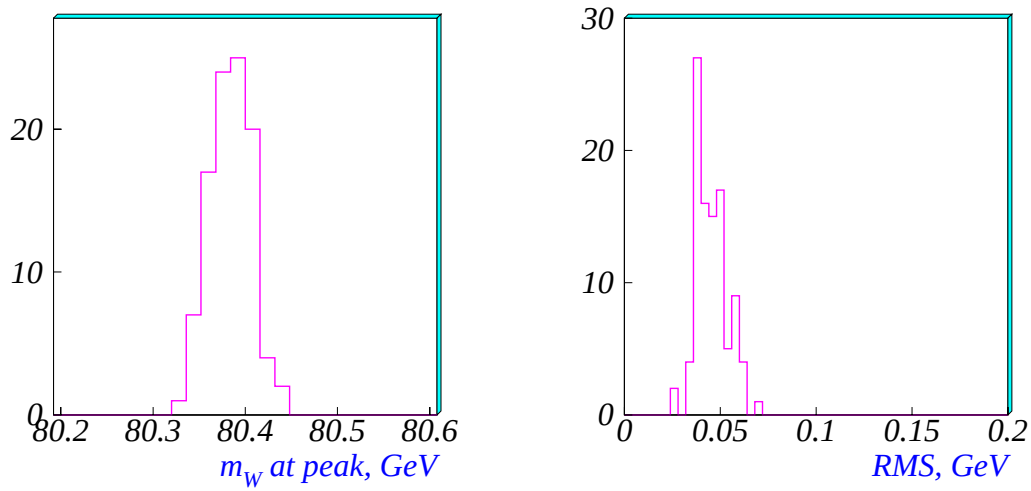

Figure 5.13: Mean (left) and RMS (right) values of the Kolmogorov–Smirnov probability function. The mean and r. m. s. values for the left and right plots are 80.384 ± 0.023 GeV and 0.045 ± 0.008 GeV, respectively

Chapter 6

Data Analysis and Study of Systematics

6.1 Data Selection

The ratio method analysis uses the same W and Z data samples as the standard W mass analysis [5]. The samples were selected from the $82\,\mathrm{pb}^{-1}$ of data collected during the 1994–1995 Tevatron run.

6.1.1 Online Event Selection

6.1.2 Kinematic Cuts on Electron Candidates

The offline selection of W and Z candidates starts from selection of electron candidates in the events. An electron candidate is required to meet the following criteria:

- A cluster in the EM calorimeter with $E_{\mathrm{T}} \geq 25\,\mathrm{GeV}$ in the central region or $E_{\mathrm{T}} \geq 30\,\mathrm{GeV}$ in the forward region.
- A significant fraction (at least 90%) of the cluster energy in the EM calorimeter.
- The isolation fraction defined by Equation 3.6 is less than 15%.
- The shape of the cluster is consistent with the electromagnetic shower: the H matrix χ^2 defined by Equation 3.8 is required to be less than 100.
- A matching track in the EC: variable σ_{trk} defined by Equation 3.9 required to be less than 10.

6.1.3 Fiducial Cuts

In addition to the above, electron candidates are required to be in the regions of well understood response of the detector. This gives rise to the following set of fiducial cuts:

- $|\eta| < 1.1$ or $1.5 < |\eta| < 2.5$. This requirement excludes the inter-cryostat region and the very forward region close to the beam pipe.

- The angular position of the electron cluster in the central calorimeter is required to be at least 10% of the module size away from the boundaries of the calorimeter modules.

- The z coordinate of the track centroid in the CDC is constrained to be within ± 80 cm from the origin to exclude nonlinearity regions of the CDC delay lines.

6.1.4 Event Selection Criteria

The following requirements are applied to the W candidates:

- At least one electron candidate.

- $\not{E}_{\mathrm{T}} \geq 25\,\mathrm{GeV}$ if the electron candidate is in the central region or $\not{E}_{\mathrm{T}} \geq 30\,\mathrm{GeV}$ otherwise.

- $p_{\mathrm{T}}^{\mathrm{boson}} \leq 30\,\mathrm{GeV}$.

Z events are selected according to the following criteria:

- At least two electron candidates.

- At least one has a matching track.

- $p_{\mathrm{T}}^{\mathrm{boson}} \leq 30\,\mathrm{GeV}$.

- No significant missing energy in the event ($\not{E}_{\mathrm{T}} \leq 15\,\mathrm{GeV}$).

Unlike the conventional DØ W mass analysis, the ratio method uses a more relaxed cut on the boson transverse momentum since the effect of the boson production model on the transverse mass cancels in the m_{T} ratio.

Figs. 6.1 and 6.2 show the data *vs.* the CMS Monte Carlo comparison for the electron p_{T} and η distributions for the W and Z samples for the same set of kinematic and fiducial cuts with the CC *vs.* EC efficiency correction weights but without the η dependent acceptance weight.

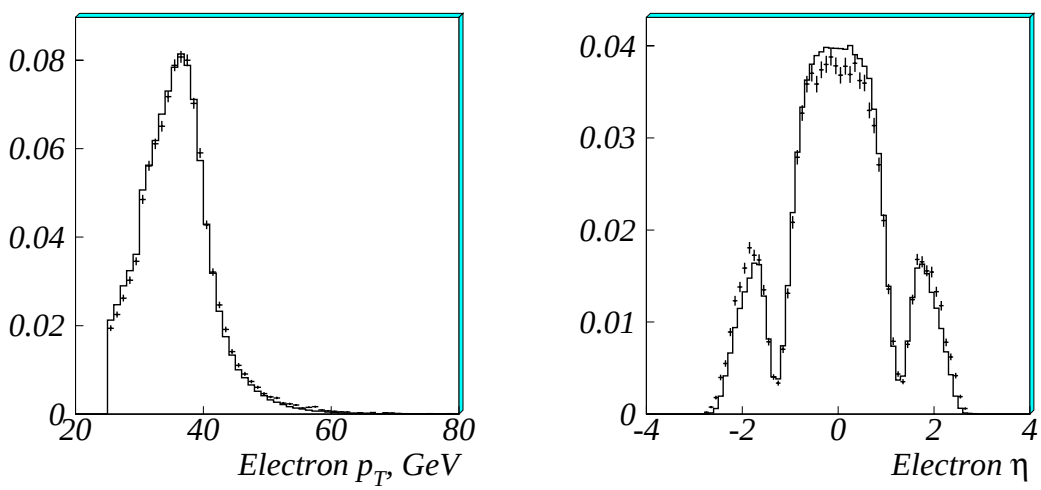

Figure 6.1: W electron p_{T} and η distributions. Solid histogram — CMS Monte Carlo, points — data

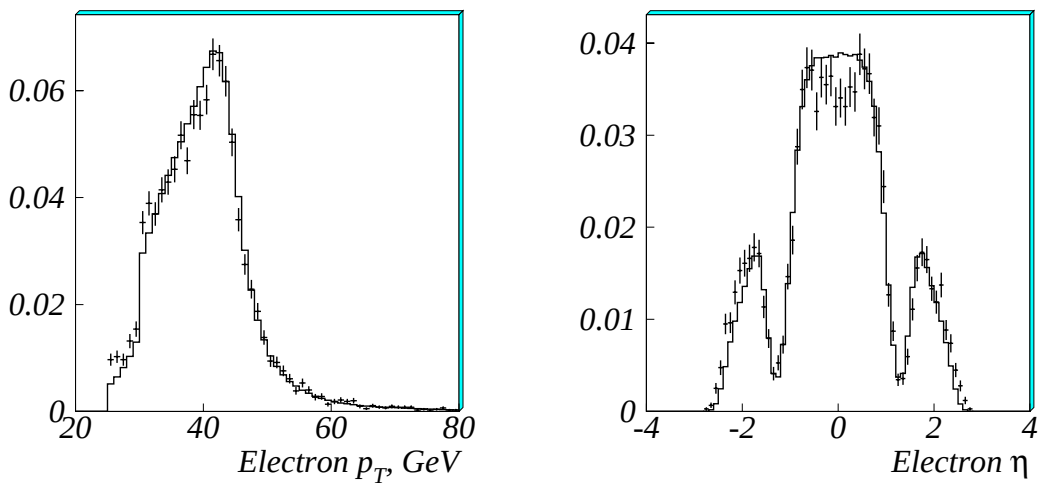

Figure 6.2: Z electron p_{T} and η distributions. Solid histogram — CMS Monte Carlo, points — data

6.2 Kolmogorov–Smirnov Fit for the Data

After the selection cuts described above, 33137 W and 4588 Z events remain in the samples[1].

The transverse mass distributions used in the Kolmogorov–Smirnov fit are shown in Fig. 6.2. Fig. 6.2 shows the transverse momenta of W and Z, and Fig. 6.5 those of the decay products. The pseudorapidity distributions of the W and Z electrons are shown in Fig. 6.2. Similar to the Monte Carlo figures, the bottom plots show the bin by bin difference between the corresponding distributions for the W and Z events.

[1]The exact number of events varies from one smearing iteration to another. This variation is of the order of ~ 10 events.

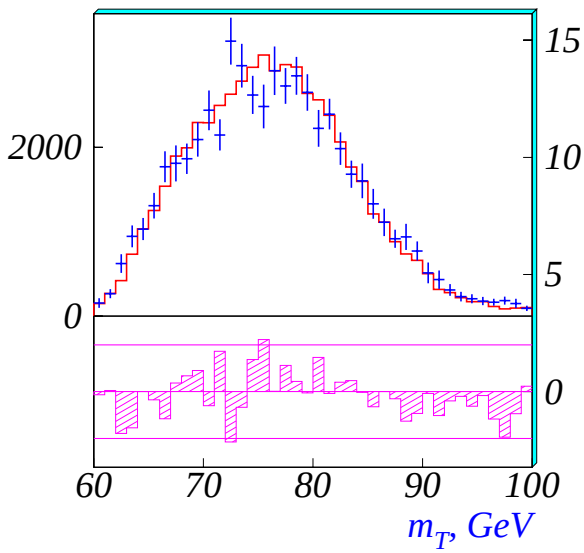

Figure 6.3: Transverse mass of the W boson (solid) and scaled transverse mass of the Z boson (dots)

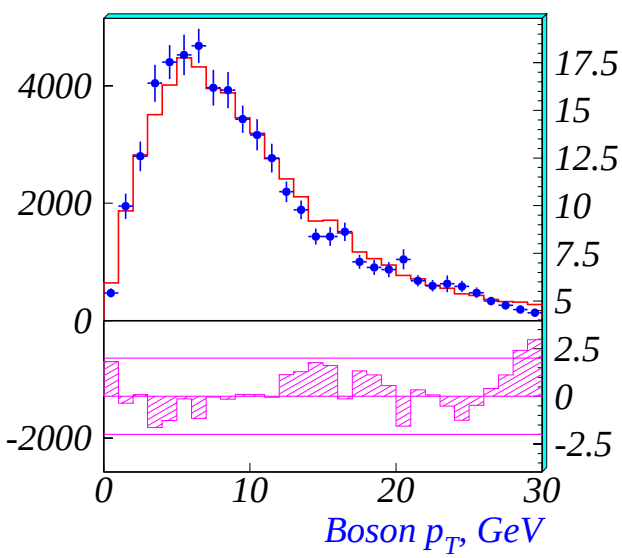

Figure 6.4: Transverse momentum of the W and Z (scaled) bosons

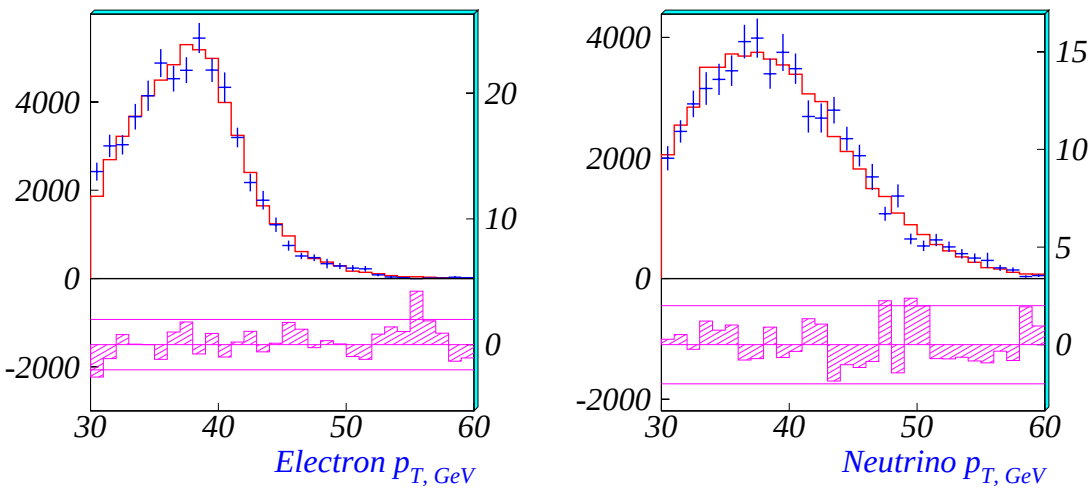

Figure 6.5: Left — p_{T} of the electron, right — p_{T} of the W neutrino on top of p_{T} of the second Z electron. Z distributions are scaled down by the mass ratio

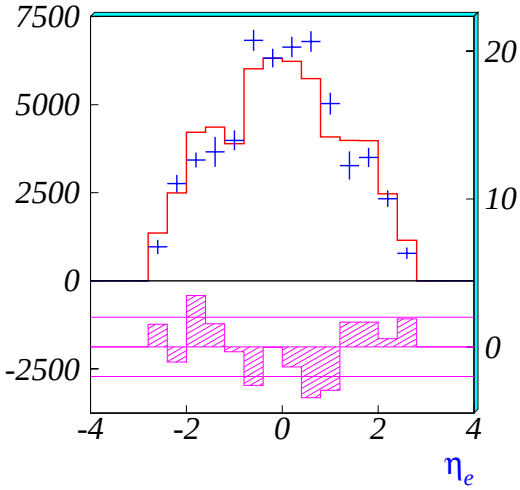

Figure 6.6: Pseudorapidity of the W and Z electrons

The W mass value at maximum of the Kolmogorov–Smirnov probability and the width of the probability function for 100 smearing iterations are plotted in Figure. 6.7.

The two distributions were fitted to a Gaussian and the mean values of the fit are interpreted as the output W mass and the statistical error, respectively:

$$m_W = 80.115 \pm 0.211\,\text{GeV}. \tag{6.1}$$

It should be mentioned that if no θ or ϕ dependent weights are applied to the data, the W mass value comes out lower than the value above by approximately the same amount as seen in the Monte Carlo (Figure 5.7).

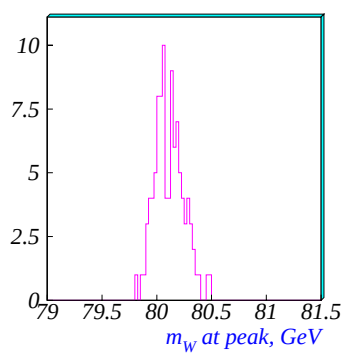

Fit results:

$$\text{Mean} = 80.115\,\text{GeV}$$

$$\sigma = 0.132\,\text{GeV}$$

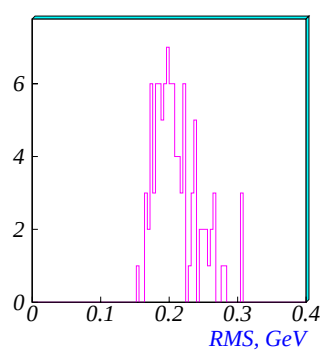

Fit results:

$$\text{Mean} = 0.211\,\text{GeV}$$

$$\sigma = 0.033\,\text{GeV}$$

Figure 6.7: Mean (top) and RMS (bottom) values of the Kolmogorov–Smirnov probability function

As a cross check for the statistical error, an ensemble test was performed using a set of CMS Monte Carlo samples (50 (W, Z) sample pairs) with numbers of events approximately equal to those of the data W and Z samples for the input W mass of 80.4 GeV. The distribution of the output Monte Carlo W mass values over the ensemble is shown in Figure 6.2 and is consistent with the statistical error of 211 MeV obtained from the data.

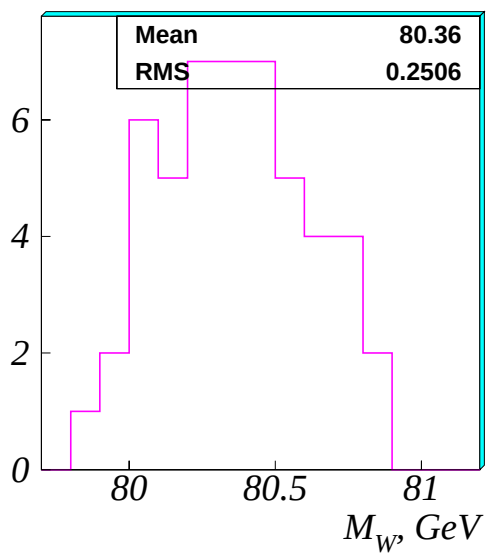

Figure 6.8: Distribution of the output Monte Carlo W mass for 50 (W, Z) sample pairs of approximately the same sizes as data for the input mass of 80.4 GeV.

6.3 Systematic Uncertainties

6.3.1 W and Z Production and Decay

The sources of theoretical model uncertainties that affect the W mass measurement are:

- W boson width,
- Parton distribution functions,
- Boson p_{T} distribution (parameter g_2 in Equation 4.5),
- Final state radiation.

A systematic error due to each of these effects was obtained using a set of CMS Monte Carlo experiments with variations of the corresponding parameter of the model described in [34] in detail. Large samples of a few million events were used for the study of systematics to minimize the statistical uncertainty. A modified Kolmogorov–Smirnov procedure in which the two transverse mass distributions were stored as histograms, not as collections of individual events, had to be used because of the computer memory constraint. The bin size of these distributions was set to 5 MeV. It was shown at a smaller sample that both binned and unbinned fit give the same result with such a bin size.

The uncertainty due to the W width has been studied by generating a set of the W CMS Monte Carlo samples for a set of variations of Γ_W. The nominal width value used for the estimate was [4]:

$$\Gamma_W = 2.06 \pm 0.05\mathrm{GeV}. \tag{6.2}$$

The dependence of the output W mass *vs.* Γ_W is shown in Table 6.1.

Γ_W, GeV	m_W, GeV
1.7	80.404
1.9	80.410
2.06	80.411
2.3	80.417
2.5	80.421

Table 6.1: W mass *vs.* Γ_W dependence. Each mass value from the right column carries a Monte Carlo statistical error of 10 MeV. This uncertainty is added in quadrature to the total systematic error.

The pdf uncertainty was modeled by substituting boson p_{T} *vs.* η grids in the CMS Monte Carlo for the MRSA, MRSD$-'$, and CTEQ2M parton distributions. Table 6.2 shows the dependence of the output W mass *vs.* the choice of the parton distribution. The overall uncertainty of 10 MeV was assigned. The uncertainty due to the boson p_{T}

pdf	m_W, GeV
MRSA	80.410
MRSD$-'$	80.397
CTEQ2M	80.418

Table 6.2: W mass *vs.* dependence on the parton distribution function. Each mass value has a 10 MeV error due to Monte Carlo statistics.

distribution was obtained by varying the g_2 parameter by its one standard deviation within the MRSD$-'$ parton distribution. An error of 5 MeV was assigned to the W mass.

The error due to the final state radiation is determined by the cuts on parameters $E^{\gamma}_{\mathrm{min}}$ and $\Delta R^{\gamma}_{\mathrm{min}}$ in the Monte Carlo [33]. These parameters are the minimum photon

energy and separation from the electron in (η, φ) space at which the photon is detected in the calorimeter. Table 6.3 shows the offsets in the output W mass due to the variations of $\Delta R^{\gamma}_{\rm min}$ (shifts due to $E^{\gamma}_{\rm min}$ variations are consistent with zero).

$\Delta R^{\gamma}_{\rm min}$ (CC)	$\Delta R^{\gamma}_{\rm min}$, cm (EC)	Δm_W, MeV
0.3	20	0
0.1	20	45
0.5	20	-9
0.3	15	26
0.3	25	-5

Table 6.3: m_W shift due to variations of the final state radiation parameters

Table 6.4 summarizes the systematic errors due to the theoretical model uncertainties.

Variable	Δm_W, MeV
W boson width Γ_W	5
Parton Distributions	10
Boson $p_{\rm T}$ (g_2)	5
Final state radiation	10
Total	16

Table 6.4: Systematic errors on the W mass due to theoretical uncertainties

6.3.2 Detector Response Parameters

Similar to the conventional DØ W mass measurement, the output of the ratio method depends on the calorimeter energy scale and resolution. However, the way the un-

certainties in the detector response parameters propagate to the result is different in the two analyses. To estimate the systematic error on the W mass due to *e.g.* electromagnetic or hadronic energy scale one needs to vary these parameters within their uncertainties and perform a Monte Carlo fit for a set of such variations [34]. In the ratio method the detector response parameter enter as corrections to the measured transverse momenta of the electrons and the recoil in a well defined analytical way (Equations 5.2, 5.10, and 5.5). It is therefore possible to calculate partial derivatives of m_W with respect to the response parameters analytically thus estimating the systematic uncertainties from the detector response. A previous study by S. Rajagopalan and M. Rijssenbeek [45] shows that the uncertainties obtained by analytical method agree with those obtained through the Monte Carlo simulation.

Using Equations 5.2 and 5.10, the square of the transverse mass of the W boson can be written as:

$$\begin{aligned} m_{\mathrm{T}}^2(W) &= 2\frac{(E_{\mathrm{T}}^e - U^{\mathrm{ue}} + U^{\mathrm{zs}})}{\alpha}(1-\cos(\varphi^e - \varphi^\nu)) \\ &\times \frac{1}{\delta}\left|\vec{\not{E}}_{\mathrm{T}} + \vec{U} + \vec{E}_{\mathrm{T}}^e\left(1 - \frac{U^{\mathrm{ue}}}{E_{\mathrm{T}}^e}\right) - \frac{\delta\vec{E}_{\mathrm{T}}^e(E_{\mathrm{T}}^e - U^{\mathrm{ue}} + U^{\mathrm{zs}})}{\alpha E_{\mathrm{T}}^e}\right|. \end{aligned} \tag{6.3}$$

Similarly, the square of the Z transverse mass from Equations 5.10 and 5.5 is given

by:

$$
\begin{aligned}
m_{\mathrm{T}}^2(Z) &= 2\frac{(E_{\mathrm{T}}^{e_1} - U^{\mathrm{ue}_1} + U^{\mathrm{zs}})}{\alpha}(1-\cos(\varphi^{e_1} - \varphi^{e_2})) \\
&\times \frac{1}{\delta}\left|\vec{\not{E}}_{\mathrm{T}} + \vec{U} + \vec{E}_{\mathrm{T}}^{e_1}\left(1 - \frac{U^{\mathrm{ue}_1}}{E_{\mathrm{T}}^{e_1}}\right) - \frac{\delta \vec{E}_{\mathrm{T}}^{e_1}(E_{\mathrm{T}}^{e_1} - U^{\mathrm{ue}_1} + U^{\mathrm{zs}})}{\alpha E_{\mathrm{T}}^{e_1}}\right. \\
&+ \left.\vec{E}_{\mathrm{T}}^{e_2}\left(1 - \frac{U^{\mathrm{ue}_2}}{E_{\mathrm{T}}^{e_2}}\right) - \frac{\delta \vec{E}_{\mathrm{T}}^{e_2}(E_{\mathrm{T}}^{e_2} - U^{\mathrm{ue}_2} + U^{\mathrm{zs}})}{\alpha E_{\mathrm{T}}^{e_2}}\right|,
\end{aligned}
\tag{6.4}
$$

The ratio of the transverse masses of the W and Z bosons can be rewritten as:

$$
\frac{m_{\mathrm{T}}(W)}{m_{\mathrm{T}}(Z)} = K\frac{\mu_{\mathrm{T}}(W)}{\mu_{\mathrm{T}}(Z)}, \tag{6.5}
$$

where $\mu_{\mathrm{T}}(W)$ and $\mu_{\mathrm{T}}(Z)$ are the transverse masses constructed from the measured instead of true kinematic variables, and the K factor depends on the response model parameters α, δ, U^{ue}, and U^{zs}. In order to estimate that dependence, the values of the measured electron transverse momenta and the W missing energy are assumed to be at half the value of the corresponding boson mass. The first order expansion in $U^{\mathrm{ue}}/M_{W,Z}$ gives:

$$
K = 1 - \frac{2(U^{\mathrm{ue}} - U^{\mathrm{zs}})}{M_W} + \frac{2(U^{\mathrm{ue}} - U^{\mathrm{zs}})}{M_Z} + \frac{\alpha}{\delta}\left(\frac{U^{\mathrm{ue}}}{M_W} - \frac{U^{\mathrm{ue}}}{M_Z}\right). \tag{6.6}
$$

The uncertainties in the W mass due to uncertainties in α, δ, U^{ue}, and U^{zs} can be

estimated in the following way:

$$\Delta m_W \simeq \frac{\partial m_W}{\partial x}\Delta x = \frac{\partial K}{\partial x}\Delta x, \tag{6.7}$$

where x and Δx are the variable and the corresponding uncertainty from the list of α, δ, U^{ue}, and U^{zs}.

Systematic effects due to electromagnetic and hadronic energy resolution were studied by varying the corresponding resolution parameters within one standard deviation in the Monte Carlo. The only noticeable contribution to the systematic error, 15 MeV, is due to the hadronic resolution sampling term.

An uncertainty due to different CC *vs.* EC electron efficiency was studied by simulating the event selection efficiency in a standalone program after the event generation with CMS. The W event selection efficiency was varied within its error bars (Table 5.3), and the Z efficiency was set equal to the ratio of the central values of the W to Z efficiency times the current W efficiency. A random number between 0 and 1 was generated for each event, and the event was selected if the random number came out greater than the corresponding efficiency value. The overall uncertainty was found to be 20 MeV.

The systematic errors due to detector response parameters are summarized in Table 6.5.

Variable	Δm_W, MeV
Electron energy scale α	5
Hadronic energy scale δ	0
U^{ue}	30
Zero suppression correction U^{zs}	5
Hadronic resolution	15
EC *vs.* CC efficiency	20
Total	40

Table 6.5: Systematic errors on the W mass due to the detector response uncertainties

The largest term in Table 6.5, the electron underlying energy correction, is due to the tails in the U^{ue} distributions shown in Figure 5.3. The CC *vs.* EC efficiency effect is the second largest contribution to the error because of the extreme sensitivity of the ratio method to the acceptance difference between the W and Z events. The fact that the hadronic energy resolution is a major source of error (third largest number in Table 6.5) is because of the different ways the hadronic energy enters the relations between the electron and neutrino measured and true transverse momentum. This difference does not cancel in the ratio. The hadronic energy resolution is one of the largest sources of error in the conventional DØ W mass measurement as well.

6.3.3 Backgrounds

The main backgrounds to the $W \to e\nu$ sample are the τ decays, $Z \to e^+e^-$ events where one of the electrons is lost, and QCD fakes. The effect of the backgrounds was studied by varying the normalization of their transverse mass distributions and adding them to simulated data [34, 45]. The uncertainties due to the backgrounds are given in Table 6.6. The error due to the τ background is larger in this analysis than

Background	Error on m_W, MeV
$W \to \tau\nu$	10
QCD	20
$Z \to e\not{e}$	5
Total	23

Table 6.6: Systematic errors on the W mass due to backgrounds

in the conventional DØ measurement because the CMS fit templates in the latter contain approximately the same fraction of τ decays of W as the data, whereas in the ratio method the τ contamination of the two data samples is different.

6.3.4 Summary of the Systematics

Combining the total errors from Tables 6.4, 6.5, and 6.6 and adding a 10 MeV uncertainty due to Monte Carlo statistics in quadrature, the overall systematic error on

the W mass with the ratio method is found to be:

$$\Delta^{\text{syst.}} m_W = 0.050\,\text{GeV}. \tag{6.8}$$

Chapter 7

Summary of Results and Conclusion

7.1 W Mass from the Ratio Fit and from the Standard DØ Method

A measurement of the W boson mass from a direct determination of the ratio of the transverse masses of W and Z bosons using the DØ detector at the Tevatron collider at Fermilab has been described. The analysis is based on the $W \to e\nu$ and $Z \to e^+e^-$ decay modes. The study corresponds to an integrated luminosity of $82\,\mathrm{pb}^{-1}$ acquired by the DØ detector during the Tevatron collider Run Ib (1994–1995). The data samples have been collected in both central and forward region of the detector. The

W mass is found to be:

$$m_W = 80.115 \pm 0.211\,(\text{stat.})\ \pm 0.050\,(\text{syst.})\,\text{GeV}. \tag{7.1}$$

The recently published DØ W mass from the standard method is [5]:

$$m_W = 80.482 \pm 0.091\,\text{GeV}. \tag{7.2}$$

With the limited number of W and Z events in Run I the error on the W mass from ratio method is significantly larger than the one from the conventional analysis.

7.2 The Future

Although the precision of the ratio method in Run I is statistically limited, there are possible directions one can follow to improve the error. Currently the ratio analysis does not use electron or neutrino p_{T} for the fit. As mentioned before, these variables have different sensitivity to the boson p_{T} and detector smearing and therefore would give a different breakdown of the systematic errors. A correlated error analysis would be necessary to incorporate the electron and neutrino p_{T} fits into the ratio method. The overall performance of the ratio method may improve once such an analysis is available.

Another issue that may require additional consideration is the definition of the

statistical error used in the ratio analysis. Although in the limit of large statistics the width of the Kolmogorov–Smirnov probability as a function of W mass does coincide with the r.m.s. of the distribution obtained by ensemble tests for a number of smearing iterations, the r.m.s. for the real data samples is consistently smaller than the width (see Figure 6.7). A larger value of the width has been used as a conservative error estimate so far.

In the Tevatron Run II the hadronic recoil and $\not\!\!E_{\mathrm{T}}$resolution and will deteriorate because of a higher (a factor of ~ 10) luminosity [50]. On the other hand, the electron E_{T} resolution is not expected to get much worse. Since the transverse mass is sensitive (via the boson p_{T}) to the hadronic response, the electron p_{T} may replace the transverse mass as the primary fit variable in the ratio method.

With the increase of the number of W and Z bosons produced in Run II the uncertainty of the W mass measurement is projected to be about 30 MeV [50]. The error will be dominated by systematics in both the conventional and ratio methods. Once can think of combining the two measurements; however, since the systematic effects are highly correlated in the two analyses, a significant improvement in the error on the W mass is unlikely.

Appendix A

Event Reconstruction Algorithms for the Forward Preshower Detector

A.1 General Design of the Forward Preshower Detector

The Forward Preshower Detector (FPS) is a part of the upgrade DØ detector for Run II of the Tevatron collider [51]. It is designed to improve electron and photon identification in the forward region of the DØ detector ($1.5 < |\eta| < 2.5$) both at the trigger level and offline [52].

There are two identical FPS detectors in the upgrade DØ located at the north and south end calorimeters. Each FPS detector consists of finely segmented scintillator modules arranged in pairs of stereo layers (u and v) both upstream and downstream of a lead absorber. Figure A.1 shows the quarter view of the FPS detector in the $r-z$ plane. The scintillator modules are shaped as spherical wedges with the curvature

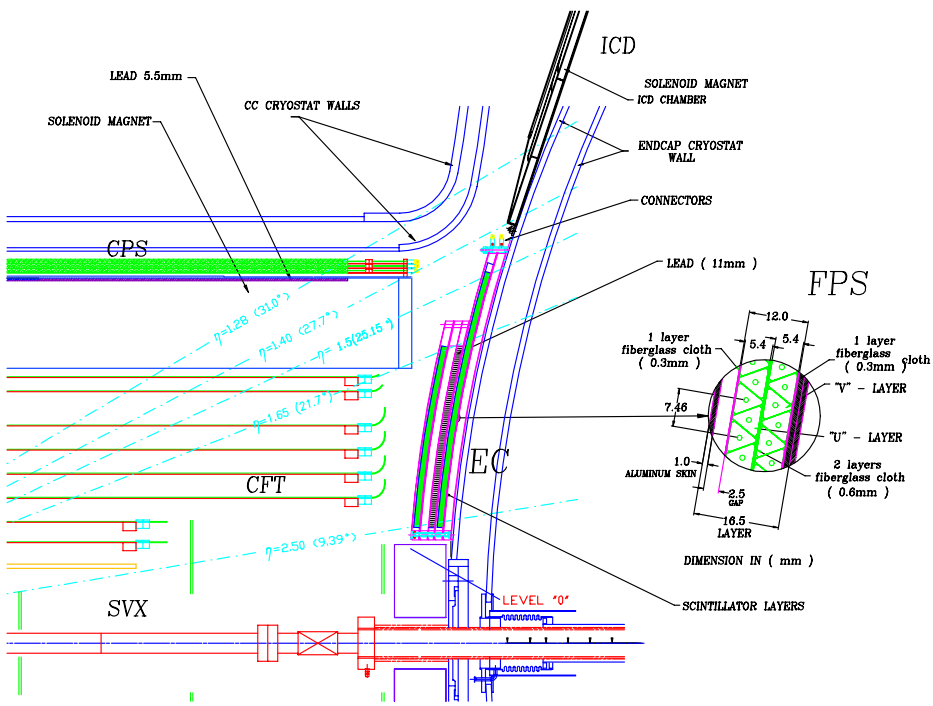

Figure A.1: FPS detector quarter view in the $r-z$ plane and a close-up view of two layers of triangular scintillator strips

radius equal to that of the inner cryostat wall of the end calorimeter. Each u and v layer of the wedge consists of nested triangular scintillator strips with a base of $\simeq 7\,\mathrm{mm}$ and a height of $\simeq 5\,\mathrm{mm}$.

Figure A.2 shows a planar projection of stereo layer u of a FPS wedge. The projection of the other layer, v, is a mirror image with respect to the x axis. The origin of the local coordinate system of the wedge is chosen at the spherical center of curvature, the z axis intersects the module at its geometrical center.

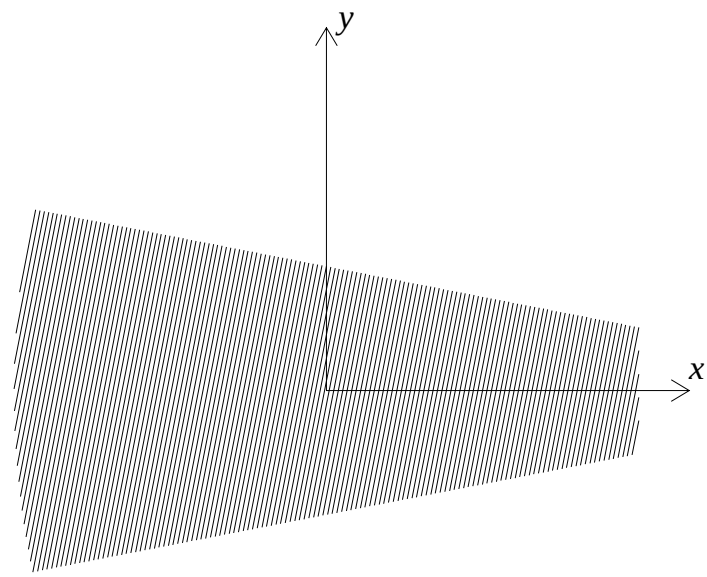

Figure A.2: Schematic $x - y$ view of strips of one stereo layer of a FPS module. The z axis is perpendicular to the plane of the drawing and completes the right-handed system.

A.2 FPS Event Reconstruction Process

The offline event reconstruction in the FPS is a four step procedure [53]. Steps 1 through 3 are performed independently for each module in the local coordinate system of the module.

1. Contiguous sets of strips with energies over a specified threshold are combined into *channel clusters* separately in u and v layers.

2. For each crossing of a channel cluster in layer u with energy over a given threshold with one in layer v a *reconstructed cluster* candidate is created. First, energy weighted average positions of the strip ends forming the channel clusters are calculated in the local coordinates of the wedge:

$$\vec{r}^{1,2} = \frac{\sum_{i=0}^{N-1} E_i \vec{r}_i^{1,2}}{\sum_{i=0}^{N-1} E_i}. \tag{A.1}$$

These two points define arcs of the great circles on the sphere. The intersection point of the arc corresponding to the channel cluster in the u layer with one in the v layer is given by:

$$\begin{aligned} \vec{R}^{\text{hit}} &= (\vec{r}_u^1 \times \vec{r}_u^2) \times (\vec{r}_v^1 \times \vec{r}_v^2), \\ \vec{r}^{\text{hit}} &= \frac{r_{\text{inner}} + r_{\text{outer}}}{2|\vec{R}^{\text{hit}}|} \vec{R}^{\text{hit}}, \end{aligned} \tag{A.2}$$

where r_{inner} and r_{outer} are the inner and the outer spherical radii of the wedge (*i.e.* hit points are bound to be located at the middle spherical surface of the wedge). Figure A.3 shows the intersection point of the u and v channel clusters.

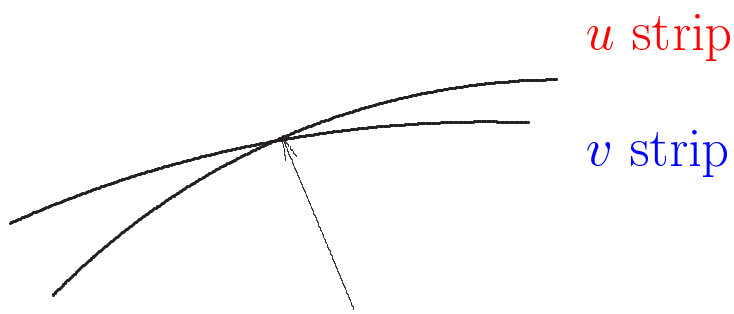

Figure A.3: Intersection point of a u and a v cluster

3. The candidates are inversely ordered by the $u-v$ energy correlation parameter

$$C_{uv} = 1 - \frac{|E_u - E_v|}{E_u + E_v}, \tag{A.3}$$

   and only top few on the list are kept depending on the threshold.

4. Positions of the reconstructed clusters are converted into the global DØ coordinates and clusters on each side within a set of (θ, φ) windows (usually defined by the calorimeter seeds) are combined into a set of collections.

The offline procedure for the initial strip clustering in the u and v layers is similar to the one used for the trigger while the rest of the algorithms are significantly different from those used online. At the trigger level computation time is a crucial issue, therefore lookup tables or simple polynomial approximations are used for the $(u, v) \rightarrow (x, y, z)$ conversion, and preshower *vs.* calorimeter clusters are only matched to the accuracy of the trigger tower size in the (η, φ) space [54, 55].

The FPS event reconstruction is a constituent part of the electromagnetic object identification and reconstruction procedure called `EMReco` which uses information from the calorimeter, preshower detectors, tracking, and vertexing algorithms to identify electrons and photons and measure their four-momenta [56].

A.3 Software Implementation

A.3.1 Hierarchy of FPS Offline Packages

The FPS event reconstruction code consists of several software packages written in C++ and interfaced with the general Run II DØ software environment [57]. The low level base packages include:

`fps_address`

Contains utility classes identifying detector modules, individual channels, and collections of channels (clusters).

`fps_event`

Holds container classes for digitized FPS data.

`fps_unpdata`

FPS part of the unpacked data chunk.

The higher level packages are:

`fps_geometry`

Alignment interface, strip position information for $(u, v) \rightarrow (x, y, z)$ conversion, and material information for the multiple scattering.

`fps_reco`

Channel and position cluster reconstruction package.

`fps_analyze`

FPS analysis and Monte Carlo *vs.* reconstruction comparison package.

`fps_display`

FPS detector and event display.

`fps_display_fwk`

Framework interface for the event display program.

A.3.2 FPS Geometry Description

Detector geometry description is an essential component of the reconstruction software [58]. `fps_geometry` package describes positions of the FPS modules in terms of rotations and offsets from the global DØ frame of reference, specifies location of individual strips with respect to the modules, implements the alignment interface and material description defined by the DØ geometry system, and provides a method to convert a pair of crossing (u, v) strips into a point and error matrix in the global

frame of reference.

The base FPS geometry tree is shown in Figure A.4. The two FPS units on either side of the DØ detector are combined logically into the FPS base geometry object. Each unit is referenced to the corresponding EC cryostat and consists of four active layers and a lead absorber layer, and each active layer holds eight modules (or wedges). Such structure ensures that a movement of a parent element of the tree due to alignment corrections gets automatically translated to the daughter elements.

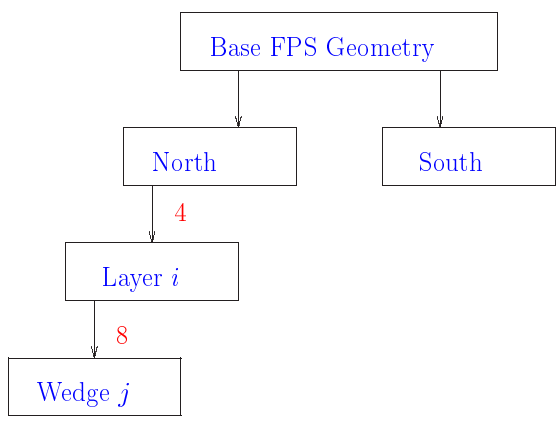

Figure A.4: FPS geometry tree. The two identical top level branches correspond to the north and south FPS detectors (only the north is shown). Each detector unit has four "daughter" layers, and each layer holds eight "daughter" wedges.

Positions of individual strips on the modules are calculated and stored in the object called the channel geometry. It is the channel geometry that implements the $(u, v) \rightarrow (\varphi, \theta)$ conversion method defined in Equation A.2 in the local coordinate system of the module.

A.4 Algorithm Performance

FPS reconstruction has been tested using single electron Monte Carlo samples with $p_{\mathrm{T}} = 50\,\mathrm{GeV}$ generated with the Run II DØ detector simulation program called `dØgstar` [59]. Figures A.5 and A.6 show the θ and φ residuals between the positions of the energy centroids of the clusters reconstructed in the FPS and the directions of the original Monte Carlo leptons corrected for the vertex position before and after the lead absorber separately. The two distinct peaks in Figure A.6 are due to the presence of the magnetic field. The angular residual distributions were fitted with a Gaussian function for the θ angle and a double Gaussian for the ϕ. The width of each $\Delta\phi$ peak is about four times larger than that of $\Delta\theta$ because of the ratio of the two diagonals of the $u - v$ crossing diamond. The width of the θ residuals corresponds to approximately 3 mm.

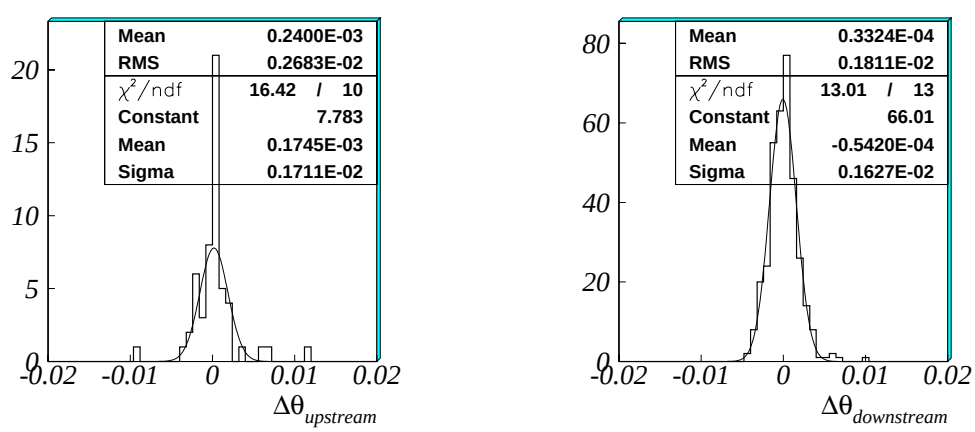

Figure A.5: Single electron θ residuals before (left) and after the lead absorber

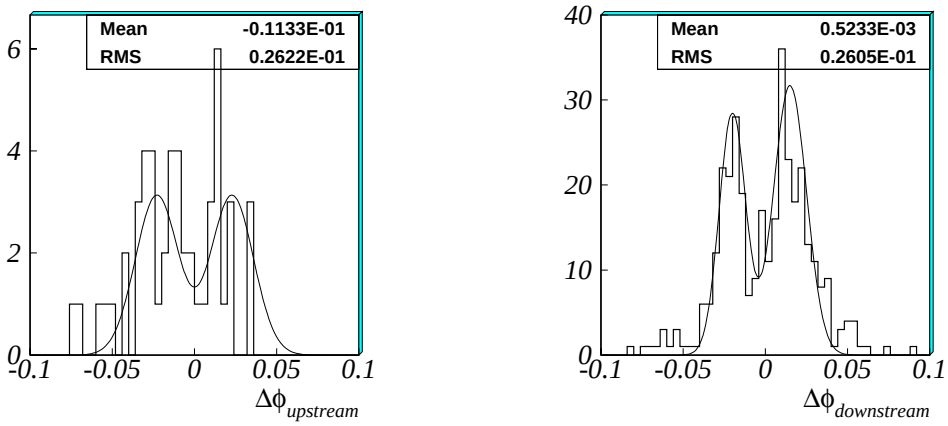

Figure A.6: Single electron φ residuals before (left) and after the lead absorber. The two peaks are due to the magnetic field

Figure A.4 shows the total energy in the event in the reconstructed clusters as a function of energy in the strips. The band located to the top of the bisector direction is due to "ghost" hit combinations. Elimination of the spurious combinations cannot be done using the preshower detector alone but requires the seed information from the calorimeter.

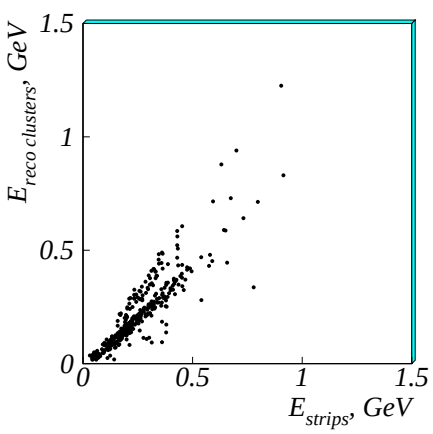

Figure A.7: Energy correlation between the reconstructed clusters and digitized strips

After filtering out the "ghosts", the energy of the preshower clusters matched to a calorimeter seed is added (with a weight factor optimized for the overall energy resolution) to the electromagnetic cluster defined by the seed. Both calorimeter seed driven elimination of "ghosts" and electromagnetic cluster energy correction for the preshower energy are carried out by the `EMReco` algorithms after the calorimeter and preshower reconstruction.

The FPS modules overlap in the global DØ (x, y) plane as shown in Figure A.8. The width of each overlap region is $\simeq 2.5\,\mathrm{cm}$.

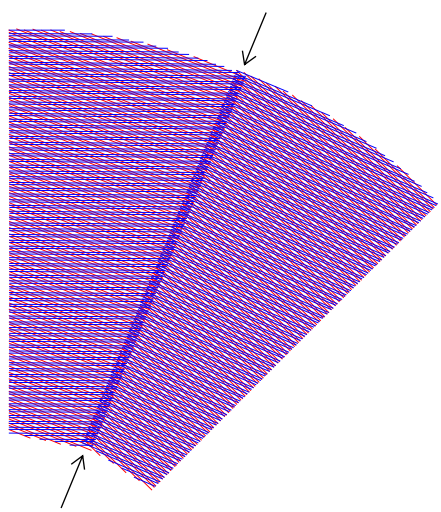

Figure A.8: FPS module overlap in (x, y) plane (global DØ coordinates)

The energy contribution from FPS clusters to the EM cluster is different in the overlap regions from the rest of the fiducial region of the detector since the number of clusters there is roughly twice greater than elsewhere in the FPS. A correct EM

energy calculation algorithm would therefore have to assign a different weight to FPS clusters in the overlap regions. A study of this issue is underway.

A.5 Conclusion

The Forward Preshower detector is an essential hardware component of the DØ detector upgrade for Run II of the Tevatron collider. Algorithms for the offline event reconstruction in the FPS have been developed and implemented in the DØ offline software framework. Performance of the FPS reconstruction program has been tested using the single particle Monte Carlo samples. Integrated tests using the calorimeter seeds and more complex Monte Carlo events are underway along with further improvements in some of the packages. The software is expected to be fully operational before the start of Run II.

Bibliography

[1] S. Glashow, Nucl. Phys. **22**, 579 (1961).

[2] A. Salam, *Elementary Particle Physics*, Ed. by N. Svartholm (Almquist and Wiksel, 1968).

[3] S. Weinberg, Phys. Rev. Lett. **19**, 1264 (1967).

[4] C. Caso *et al.*, The European Physical Journal **C3**, 1 (1998).

[5] B. Abbott *et al.*, Phys. Rev. Lett. **84**, 222 (2000)

[6] The LEP Collaborations, the LEP Electroweak Working Group, and the SLD Heavy Flavor Group, Report No. CERN–PPE/97–154 (unpublished).

[7] W. J. Marciano and A. Sirlin, Phys. Rev. Lett. **61**, 1815 (1988).

[8] M. Veltman, Acta Phys. Pol. **B8**, 475 (1977).

[9] F. Halzen, B. Kniehl, and M. L. Stong, Z. Phys. **C58**, 119 (1993).

[10] R. K. Ellis, W. J. Stirling, and B. R. Webber, *QCD and Collider Physics* (Cambridge University Press, 1996).

[11] F. Abe *et al.*, Phys. Rev. **D52**, 4784 (1995).

[12] S. Abachi *et al.*, Phys. Rev. Lett. **77**, 3309 (1996).

[13] S. Abachi *et al.*, Phys. Rev. Lett. **79**, 1197 (1997).

[14] Chris Quigg, *The Top Quark and Higgs Boson at Hadron Colliders*, FERMILAB–CONF–98/059–T (1997).

[15] D. Pierce *et al.*, *Precision Corrections in the Minimal Supersymmetric Standard Model*, SLAC–PUB–7180 (1996).

[16] S. D. Drell and T. M. Yan, Phys. Rev. Lett. **25**, 316 (1970).

[17] Jamal Tarazi, *A Measurement of the Cross Section Ratio of the W and Z Electronic Decays and the Total Width of the W with the DØ Detector*, Ph. D. Dissertation, University of California at Irvine (unpublished) (1997).

[18] R. Hamberg, W. L. van Neerven, and T. Matsuura, Nucl. Phys. **B359**, 343 (1991).

[19] E. Mirkes and J. Ohenmus, Phys. Rev. **D50**, 5692 (1994).

[20] J. Collins and D. Soper, Phys. Rev. **D16**, 2219 (1977).

[21] H. T. Edwards, *Annual Review of Nuclear and Particle Science*, ed. by J. D. Jackson (Annual Reviews, Palo Alto, CA, 1985).

[22] S. Abachi *et al.*, Nucl. Instr. and Methods **A338**, 185 (1994).

[23] J. Detoeuf *et al.*, Nucl. Instr. and Methods **A279**, 310 (1989).

[24] R. Wigmans, Nucl. Instr. and Methods **A259**, 389 (1987).

[25] S. Abachi *et al.*, Nucl. Instr. and Methods **A324**, 53 (1993).

[26] `ZEBRA`, CERN program library long write up, Q100 and Q101 (1995).

[27] S. Youssef, Comp. Phys. Comm. **45**, 423 (1987).

[28] N. Graf, DØ Internal Note 1352 (1992).

[29] R. Engelmann *et al.*, Nucl. Instr. and Methods **A216** 45 (1983).

[30] U. Heintz *et al.*, DØ Internal Note 2355 (1994).

[31] UA1 collaboration, Phys. Lett. **B123**, 115 (1983).

[32] V. Daniel Elvira *et al.*, DØ Internal Note 3139 (1996).

[33] Eric Flattum, *A Measurement of the W Boson Mass in $p\bar{p}$ Collisions at $\sqrt{s} =$ 1.8 TeV*, Ph. D. Dissertation, Michigan State University (unpublished) (1996).

[34] Ian Adam, *Measurement of the W Boson Mass with the DØ Detector Using the Electron E_{T} Spectrum*, Ph. D. Dissertation, Columbia University (unpublished) (1997).

[35] J. C. Collins, D. E. Soper, and G. Sterman, Nucl. Phys. **B250**, 199 (1985).

[36] P. B. Arnold and M. H. Reno, Nucl. Phys. **B319**, 37 (1989). Erratum, Nucl. Phys. **B330**, 284 (1990).

[37] J. C. Collins and D. E. Soper, Nucl. Phys. **B193**, 381 (1981).

[38] P. B. Arnold and R. P. Kauffman, Nucl. Phys. **B349**, 381 (1991).

[39] G. A. Ladinsky and C. P. Yuan, Phys. Rev. **D50**, 4239 (1994).

[40] M. Seymour, `HERWIG` *for Hadron–Hadron Physics*, LU–TP–93–10 (1993).

[41] F. A. Berends and R. Kleiss, Z. Phys. **C27**, 365 (1985).

[42] F. Paige and S. Protopopescu, *ISAJET 5.20: A Monte Carlo Event Generator for pp and $p\bar{p}$ Reactions*, BNL–38034 (1996).

[43] J. Smith *et al.*, Phys. Rev. Lett. **50**, 1738 (1983).

[44] B. Abbott *et al.*, Phys. Rev. **D58**, 092003 (1998).

[45] S. Rajagopalan and M. Rijssenbeek, *Measurement of the W mass using the transverse mass ratio of the W and the Z*, DØ Internal Note 3000 (1996).

[46] Leopold Schmetterer, *Introduction to Mathematical Statistics*, (Springer–Verlag, 1974).

[47] Edward J. Dudewicz and Satya N. Mishra, *Modern Mathematical Statistics*, (John Wiley & Sons, 1988).

[48] B. Abbot *et al.*, Phys. Rev. **D60**, 52003 (1999).

[49] I. Adam, E. Flattum, and U. Heintz, DØ Internal Note 3198 (1997).

[50] D. Amidei and R. Brock, *Future Electroweak Physics at the Fermilab Tevatron: Report of the TeV 2000 Study Group*, (Fermilab, 1996).

[51] DØ Collaboration, *The DØ Upgrade. The Detector and its Physics*, FERMILAB–PUB–96–357–E (1996).

[52] A. Gordeev *et al.*, DØ Internal Note 3445 (1998).

[53] D. Shpakov, DØ Internal Note 3664 (1999).

[54] A. Lucotte and M. Bhattacharjee, DØ Internal Note 3493 (1999).

[55] M. Bhattacharjee, DØ Internal Note 3614 (1999).

[56] `http://www-d0.fnal.gov/d0dist/dist/releases/current/emreco/doc/EMReco.ps`

[57] W. Merritt, DØ Internal Note 3351 (1997).

[58] `http://d0server1.fnal.gov/projects/OfflineCalibAlign/home.html`.

[59] Y. Fisyak, J. Womersley, DØ Internal Note 3191 (1997).